Summer 2012

Control oriented thermal modeling of lithium ion batteries

Derek Brown

Department:

CONTROL ORIENTED THERMAL MODELING OF LITHIUM ION BATTERIES

by

DEREK BROWN

A THESIS

Presented to the Faculty of the Graduate School of the

MISSOURI UNIVERSITY OF SCIENCE AND TECHNOLOGY

In Partial Fulfillment of the Requirements for the Degree

MASTER OF SCIENCE IN MECHANICAL ENGINEERING

2012

Approved by

Robert G. Landers, Advisor
Kelly O. Homan
Mehdi Ferdowsi

PUBLICATION THESIS OPTION

This thesis has been prepared in the style utilized by the IEEE TRANSACTIONS ON ENERGY CONVERSION. Pages 9-49 will be submitted for publication in that journal. Appendices A, B, and C have been added for purposes normal to thesis/dissertation writing.

ABSTRACT

Lithium ion batteries have been widely used in consumer electronics and are beginning to move to the forefront of the automotive and power grid industries. Lithium ion batteries are desirable in these applications because they are high energy density and high specific energy cells, while remaining inexpensive and lightweight. Safety is a concern in every consumer application; therefore, in order for lithium ion battery use to continue growing, advances in battery management systems are needed. Thermal management of lithium ion batteries is currently a critical issue. Applications are becoming more dependent on active liquid thermal management systems. The development of precise battery active liquid thermal management systems begins with an accurate temperature model applicable to control design. This work is focused on the development of a dynamic active liquid cooled battery cell thermal model through the coupling of a lumped energy balance and a single particle electrochemical heat generation model. A fluid channel is added to the bottom of the cell and an aluminum heat sink is added to the side of the cell. Results demonstrate that fluid temperature has more effect on the cell temperature than fluid mass flow rate. The dynamic model developed in this work has an order of 135 and; therefore, is not applicable to controller design. Linearization about an equilibrium trajectory and model order reduction via the Global Arnoldi Algorithm (GAA) is applied. Results show good agreement between the first order reduced system and the non-linear system.

ACKNOWLEDGMENTS

First of all I would like to thank my advisor, Robert Landers, for his time and patience. Without him this publication would not be possible. He provided me with funding through a graduate teaching assistantship, which allowed me to complete my goals.

I would also like to thank my committee members, Kelly Homan and Mehdi Ferdowsi, for taking the time out of their schedules to review my work and provide feedback. Thank you Kelly for helping out with the thermal modeling and thanks to both Kelly and Mehdi for attending my defense.

I would like to thank my parents, without their encouragement and financial support; I would not be where I am today. Additionally, I would like to thank my wonderful fiancé for being so understanding and supportive.

TABLE OF CONTENTS

LIST OF ILLUSTRATIONS

LIST OF TABLES

1. INTRODUCTION

1.1. MOTIVATION

Lithium ion batteries have gained acceptance into the consumer electronic, power grid, and automotive worlds due to their high energy density and high specific energy as compared to other types of batteries in today's markets. Other advantageous properties include low self-discharge rate when not in use and the fact that lithium ion batteries exhibit no memory effect. These factors, among many others, have allowed lithium ion batteries to gain acceptance in many commercial battery applications. Lithium ion batteries are also making a strong appearance in Smart Grid applications, allowing people to receive green energy into their homes. In addition, the decrease in cost, along with the previously mentioned benefits, has propelled lithium ion batteries into the forefront of automotive applications. One of the major issues preventing lithium ion batteries from significantly penetrating the automotive and power grid markets is safety and longevity. Lithium ion batteries have specific operating conditions, with the temperature range being one of the most important constraints. Optimal operating temperatures for a lithium ion cell range from -10 to 50°C [1]. Lithium ion batteries suffering from excessive internal heat generation and extreme operating temperatures eventually fail, possibly triggering violent venting and rupture, along with the ignition of active battery materials [2]. This process is commonly referred to as thermal runaway and can be extremely deleterious when the cell is part of a lithium ion battery pack. Therefore, thermal management is a necessary component of any lithium ion battery pack. Active and passive thermal management systems are currently found in the literature and in renewable energy industries. Despite the cost and complexity, it has been proven that active liquid thermal management systems are more effective, as compared to passive systems, when extreme operating conditions are involved. An active liquid thermal management system must incorporate a controller that allows the system to adjust the temperature and mass flow rate of the fluid based on the battery pack temperature. The development of such a controller is dependent on an accurate thermal model of the pack.

1.2. DIRECTION OF WORK

The following work is targeted at predicting the thermal behavior of a lithium ion cell under different operating conditions. Once the thermal behavior of the cell can be reliably determined the next step is to apply this model to control theory. Since a detailed model is developed in this work, a method capable of reducing this model to a control oriented model is introduced. This work is separated into two distinct sections: the thermal model using a lumped energy balance approach and a control oriented thermal model obtained using linearization techniques and the Global Arnoldi Algorithm (GAA). In order to determine where efforts should be focused in the development of lithium ion battery modeling a thorough literature review was conducted. The following sections will discuss the working phenomena of a lithium ion cell followed by a summary of the selected literature review regarding thermal management of lithium ion battery packs, thermal runaway, and thermal modeling. The literature review reveals that there is much work to be done in the area of thermal control and that the need for precise temperature control of each module of the battery pack is prevalent. Correspondingly, the literature provides numerous lithium ion cell thermal models; however, these models prove to be highly complex. In order to accurately apply control theory to lithium ion battery packs a simple low order model that captures the dynamics of the cell is needed. Therefore, a discussion of the thorough literature review of model order reduction techniques will be provided. Figure 1.1 shows the progression of this work from the electrochemical equations and working physics of the battery to a control oriented reduced model which can be used to develop thermal control theory for lithium ion cells.

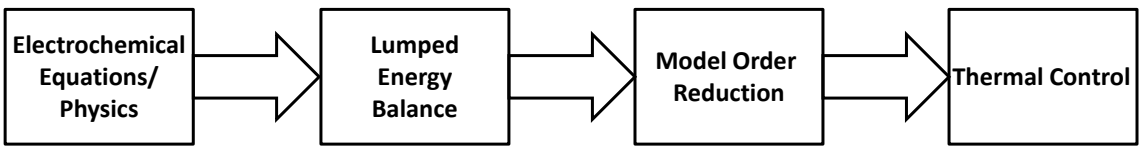

Figure 1.1. Progression of work

1.3. WORKING PHENOMENA OF A LITHIUM ION CELL

A battery cell typically consists of anywhere between 30 and 100 electrode sandwiches. Note that in this work as others, an electrode sandwich is comprised of different layers that facilitate the electrochemical process that a battery undergoes during charge and discharge. The layers in each electrode sandwich are the anode, cathode, separator, and two different current collecting materials. Figure 1.2 is a simple diagram of three neighboring electrode sandwiches.

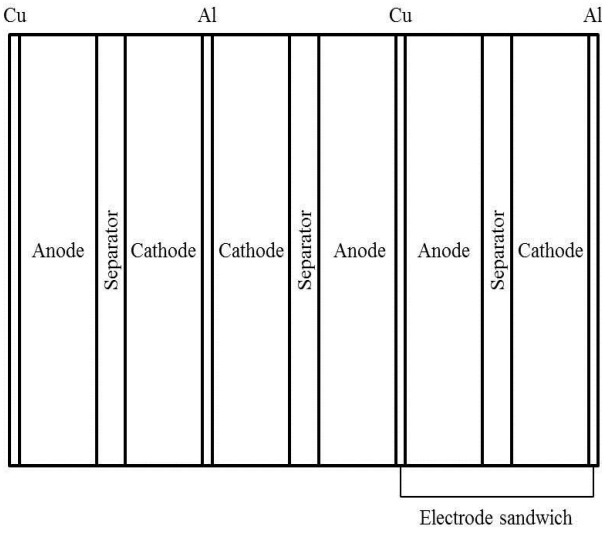

Figure 1.2. Three neighboring electrode sandwiches

The anode, or negative electrode, contains graphite and its chemical composition is typically Li_xC_6. The cathode, or positive electrode, is typically a metal oxide or a blend of metal oxides (i.e. $Li_xMn_2O_4$ or Li_xCoO_2). The separator is a porous medium that acts as an electrical insulator between the anode and the cathode by not allowing electrons to flow through. However, the separator with allow ion transfer. The current collectors are located between the anode or cathode of one electrode and the anode or cathode of the neighboring electrode. They are nonporous and assist in connecting the

porous electrode to the cell terminals. The material of the anode current collector is copper and the material of the cathode current collector is aluminum [3]. Figure 1.3 depicts the electrode sandwich and the transfer of ions during charge and discharge.

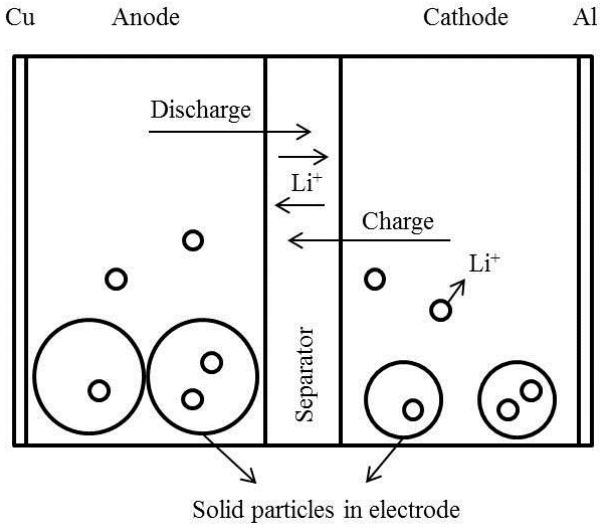

Figure 1.3. Anatomy of lithium ion intercalation cell showing charge and discharge lithium ion direction

Lithium ion cells are commonly referred to as dual-intercalation cells, meaning that both electrodes have lattice sites that can store lithium. Charging (discharging) a lithium ion cell causes the lithium ions to leave the lattice sites in the positive (negative) electrode and enter the lattice sites in the negative (positive) electrode [3]. Section 2 will explain the sources of heat generation found in lithium ion batteries along with the mode in which heat flows to the surface of the cell. The main challenge today is determining the best approach to modeling the heat generation and heat transfer within the battery. The paper entitles “Control Oriented Thermal Modeling of Lithium Ion Batteries” will provide procedures for determining cell heat generation and temperature profiles. The paper will provide the method used in this work to develop a control oriented thermal model of a lithium ion cell. Many devices, including laptops and hybrid electric vehicles

depend on accurate lithium ion battery thermal models to keep their users safe. The novelty of this work is that the model can be used to design a thermal controller that can be implemented using any lithium ion physical system.

1.4. LITERATURE REVIEW

The following subsections provide a glance at the literature for battery thermal management, thermal runaway, thermal modeling, and model order reduction.

1.4.1. Thermal Management Literature Review. Thermal management is a costly but necessary component of all lithium ion battery packs. The cost and effectiveness of the thermal management system is dependent on the type of thermal management system. Active and passive thermal management systems are currently found in literature. Active thermal management systems can use either forced air or liquid convection. Two common methods of dispensing air to a battery pack are series cooling/heating and parallel cooling/heating. Series cooling/heating involves air entering one end of the pack and leaving through the opposite end of the pack. Parallel cooling/heating splits the flow rate of the air into two equal portions and distributes that air separately to each module [4]. The debate between air and liquid thermal management systems persists today. Liquid thermal management systems are more effective in the sense that it is capable of transferring more heat from the pack to the heat transfer medium, i.e., the fluid. Liquid thermal management systems also have drawbacks. The plumbing involved with the system adds to the complexity and weight of the battery pack. The possibility of leakage arises and creates the possibility of electrical fires or battery pack failure. The complexity raises the cost of the final product as more material must be purchased and more man hours must be expended to fabricate and assemble the product. Due to the complexity and cost of active thermal management systems, passive thermal management systems have been a recent research interest. A passive thermal management system may incorporate a phase change material (PCM) encapsulated in a graphite matrix that separates the cells in a battery module. Passive cooling with PCM is said to prevent the propagation of thermal runaway within the

module [5]. The main drawback of PCM thermal management is that there is no possibility of heating the battery pack during cold start. Although, PCM has been proven to be an effective alternative, many battery packs today require operation in a wide variety of environments. There is much discussion found in literature regarding different methods of thermal management; however, little is available concerning the method and development of a thermal controller. This work will provide a control oriented thermal model of an active liquid cooled lithium ion cell that will provide the groundwork for thermal controller development and validation on a physical system.

1.4.2. Thermal Runaway Literature Review. Thermal runaway occurs in batteries when elevated temperatures trigger heat generating exothermic reactions, raising the temperature further and potentially triggering more deleterious reactions [6]. Therefore, the battery internal temperature increases rapidly if there is not a proper and effective thermal management strategy in place. Different parts of the battery behave differently at elevated temperature and the parts even begin to decompose at specific temperatures. The solid electrolyte interface (SEI) is a protection layer that guards the lithiated carbon from the organic electrolyte. The SEI layer begins to exothermically decompose at approximately 85 °C. Without an SEI layer, the negative electrode material and organic electrolyte begin to react exothermically around temperatures of 100 °C. When the temperature nears 110 °C a secondary layer begins to form and consequently decomposes. Evaporation of the electrolyte occurs at ~140 °C and the separator begins to melt between 130 and 190 °C. A melted separator can cause internal short circuits, therefore, causing more heat generation. Also, typical organic electrolytes can combust if vaporized and exposed to oxygen, which can be evolved from delithiated positive electrodes [6]. Many instances of lithium ion battery packs overheating and in some cases catching fire have been reported [7]. As the usage of lithium ion batteries in consumer electronics and vehicles continues to increase, efforts must focus on discovering new more effective and reliable ways of preserving lithium ion safety. Thermal runaway can occur when the battery is exposed to multiple types of abuse scenarios such as elevated temperatures, overcharging, internal short circuit, crushing, piercing, etc. Not only can a single cell configuration cause damage to a human being and its surroundings, but a single cell entering thermal runaway in a pack of lithium ion

cells can cause thermal runaway to propagate throughout the entire pack causing insurmountable damage to the product and people in close contact with the product. Thermal runaway has been combated using numerous different strategies. For example, the most common current limiter is a thermal fuse that will open at 30-50 °C above the maximum operating temperature of the battery, therefore, disconnecting the battery electronically from the source [7]. Another possibility of maintaining the safety of lithium ion users in hybrid electric vehicles, laptops, etc. would be to construct fireproof containers for these batteries to function in; consequently separating any disaster that might occur from its surroundings. Many of the methods available will render the battery pack of module inoperable after a cell goes into thermal runaway unless each cell is individually equipped with a thermal runway deterrent. The main goal of this work is to show that there are ways to preserve the rest of the pack when one lithium ion cell is undergoing thermal runaway. An active liquid cooled temperature controller will allow for safe operation while a single cell in a pack of cells is undergoing thermal runaway while also allowing for the misbehaving cell to be located and replaced. Accurate control oriented lithium ion thermal models are necessary to develop such control theory.

1.4.3. Thermal Modeling Literature Review. Considerable efforts have been focused on developing electrochemical-thermal coupled and one, two, and three dimensional finite element models of lithium ion batteries. Srinivasan et al. [8], Fang et al. [9], Gu et al. [10], Thomas et al. [11], and Bernardi et al. [12] have made substantial contributions to the literature with their electrochemical-thermal coupled battery models. Srinivasan et al. [8] developed a thermal-electrochemical coupled two dimensional model using a local heat generation method with parameter temperature dependence based on the Arrhenuis-type relationships. Fang et al. [9] proposed a one dimensional thermal-electrochemical coupled lumped thermal model where the temperature and current did not vary spatially. Guo et al. [13], Guo et al. [14], and Zhang et al. [15] have made contributions to the area of Single Particle heat generation modeling. Guo et al. [13] extended a single particle model to include an energy balance where the spatial temperature distribution in the cell is neglected, and the cell temperature was examined with different boundary conditions. Guo et al. [14] incorporated the single particle model into a one dimensional prismatic cell battery model. The heat transfer between cells was

determined using a set of experimentally determined contact thermal resistance values. Ma et al. [16] and Chen et al. [17] have made significant contributions to two and three dimensional battery cell finite element modeling. Ma et al. [16] proposed a three dimensional finite element approach with one set of effective thermal properties describing the entire cell. The work in this paper focuses on a two dimensional lumped energy balance of a prismatic lithium ion cell with heat generation dependent on reversible and irreversible heating obtained using a single particle electrochemical model. This thermal model, along with most thermal models found in literature, cannot easily be applied for control applications. A control oriented model that captures the dynamic characteristics of the original lumped model is needed.

1.4.4. Model Order Reduction Literature Review. Typically, control oriented battery models are developed using the combination of highly complex electrochemical-thermal coupled models and experimental parameter estimation, as is the case in the work by Bartholomaeus et al. [18]. In this work it will be shown that the development of a control oriented model using model order reduction techniques is more desirable and produces accurate results without the need of experimental testing. The Arnoldi algorithm has been applied successfully numerous times in MEMS applications. Chen et al. [19] applied the combination of the Taylor series expansion and the Arnoldi algorithm to a weakly nonlinear system and obtained good results. Lai et al. [20] applied the Global Arnoldi Algorithm (GAA) to a Multiple Input Multiple Output (MIMO) RLCG (Resistance, Inductance, Capacitance, and Conductance) system and obtained good results. This work will show that the GAA allows for the reduction of a complex high order nonlinear battery thermal model without the use of experimental data or parameter estimation. Linearization about an equilibrium trajectory is necessary to apply the GAA to this scenario. The lithium ion thermal model once represented by a large number of non-linear differential equations can now be accurately characterized by a small number of linear differential equations; thus, making the battery model applicable to controller design.

PAPER

I. Control Oriented Thermal Modeling of Lithium Ion Batteries

Derek Brown and Robert G. Landers

Abstract

Lithium ion batteries have been widely used in consumer electronics and are beginning to move to the forefront of the automotive and power grid industries. Lithium ion batteries are desirable in these applications because they have high energy density and high specific energy, while remaining inexpensive and lightweight. Safety is a concern in every consumer application; therefore, in order for lithium ion battery use to continue growing, advances in battery management systems are needed. Thermal management of lithium ion batteries is currently a critical issue. Applications are becoming more dependent on active liquid thermal management systems. The development of precise battery active liquid thermal management systems begins with an accurate temperature model applicable to control design. This work is focused on the development of a dynamic active liquid cooled battery cell thermal model through the coupling of a lumped energy balance and a single particle electrochemical heat generation model. A fluid channel is added to the bottom of the cell and an aluminum heat sink is added to the side of the cell. Results demonstrate that fluid temperature has more effect on the cell temperature than fluid mass flow rate. The dynamic model developed in this work has an order of 135; therefore, is not applicable to controller design. Linearization about an equilibrium trajectory and model order reduction via the Global Arnoldi Algorithm (GAA) is applied. Results show good agreement between the first order reduced system and the non-linear system.

I. INTRODUCTION

Lithium ion batteries have gained acceptance into the consumer electronic, power grid, and automotive worlds due to their high energy density and high specific energy as compared to other types of batteries in today's markets. Other advantageous properties include low self-discharge rate when not in use and the fact that lithium ion batteries exhibit no memory effect. These factors, among many others, have allowed lithium ion batteries to gain acceptance in many commercial battery applications. Lithium ion batteries are also making a strong appearance in Smart Grid applications, allowing people to receive green energy into their homes. In addition, the decrease in cost, along with the previously mentioned benefits, has propelled lithium ion batteries into the forefront of automotive applications. One of the major issues preventing lithium ion batteries from significantly penetrating the automotive and power grid markets is safety and longevity. Lithium ion batteries have specific operating conditions, with the temperature range being one of the most important constraints. Optimal operating temperatures for a lithium ion cell range from -10 to 50°C [1]. Lithium ion batteries suffering from excessive internal heat generation and extreme operating temperatures eventually fail, possibly triggering violent venting and rupture, along with the ignition of active battery materials [2]. This process is commonly referred to as thermal runaway and can be extremely deleterious when the cell is part of a lithium ion battery pack. Therefore, thermal management is a necessary component of any lithium ion battery pack. Active and passive thermal management systems are currently found in the literature and in renewable energy industries. Despite the cost and complexity, it has been proven that active liquid thermal management systems are more effective, as compared to passive systems, when extreme operating conditions are involved. An active liquid thermal management system must incorporate a controller that allows the system to adjust the temperature and mass flow rate of the fluid based on the battery pack temperature. The development of such a controller is dependent on an accurate thermal model.

Considerable efforts have been focused on developing detailed electrochemical-thermal coupled and one, two, and three dimensional finite element models of lithium ion batteries. Srinivasan et al. [3], Fang et al. [4], Gu et al. [5], Thomas et al. [6], and

Bernardi et al. [7] have made substantial contributions to the literature with their electrochemical-thermal coupled battery models. Srinivasan et al. [3] developed a thermal-electrochemical coupled two dimensional model using a local heat generation method with parameter temperature dependence based on the Arrhenuis-type relationships. Fang et al. [4] proposed a one dimensional thermal-electrochemical coupled lumped thermal model where the temperature did not vary spatially. Guo et al. [8], Guo et al. [9], and Zhang et al. [10] have made contributions to the area of Single Particle Modeling. Guo et al. [8] extended a single particle model to include an energy balance where the spatial temperature distribution in the cell is neglected, and the cell temperature was examined with different boundary conditions. Guo et al. [9] incorporated the single particle model into a one dimensional prismatic cell battery model. The heat transfer between cells was determined using a set of experimentally determined contact thermal resistance values. Ma et al. [11] and Chen et al. [12] made significant contributions to two and three dimensional battery cell finite element modeling. Ma et al. [11] proposed a three dimensional finite element approach with one set of effective thermal properties describing the entire cell. The work in this paper uses a two dimensional lumped energy balance of a prismatic lithium ion cell with heat generation dependent on reversible and irreversible heating obtained using a single particle electrochemical model. This thermal model, along with most thermal models found in literature, cannot easily be applied for control applications. A control oriented model that captures the dynamic characteristics of the original lumped model is needed.

Typically, control oriented battery models are developed using a combination of highly complex electrochemical-thermal coupled models and experimental parameter estimation, as is the case in the work by Bartholomaeus et al. [13]. In this work it will be shown that the development of a control oriented model using model order reduction techniques is more desirable and produces accurate results without requiring experimental testing. The Arnoldi algorithm has been applied successfully numerous times in Micro Electro-Mechanical Systems (MEMS) applications. Chen et al. [14] applied the combination of the Taylor series expansion and the Arnoldi algorithm to a weakly nonlinear system and obtained good results. Lai et al. [15] applied the Global Arnoldi Algorithm (GAA) to a Multiple Input Multiple Output (MIMO) RLCG

(Resistance, Inductance, Capacitance, and Conductance) system and obtained good results. This work will show that the GAA allows for the reduction of a complex high order nonlinear battery thermal model without the use of experimental data or parameter estimation. Linearization about an equilibrium trajectory is necessary to apply the GAA to this scenario. The lithium ion thermal model once represented by a large number of non-linear differential equations can now be accurately characterized by a small number of linear differential equations; thus, making the battery model applicable to controller design.

II. SINGLE CELL THERMAL MODEL

This section introduces a lumped energy balance approach to model the temperature distribution in a single lithium ion battery cell exposed to natural convection. In this work, a two dimensional cross-section of a prismatic lithium ion battery is analyzed (see Fig. 1).

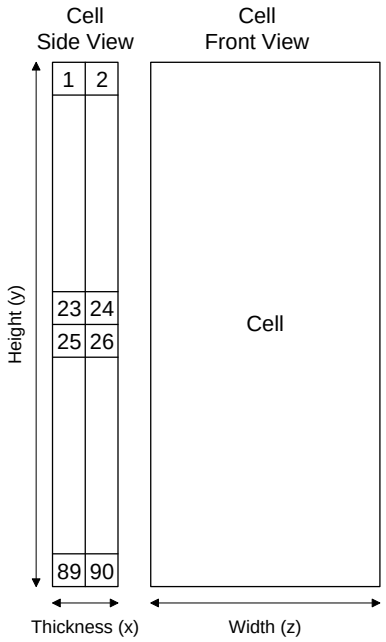

Fig. 1. Two dimensional cross-section schematic of prismatic lithium ion battery with nodes in x- (battery thickness) and y-directions (battery height).

The cell is divided into two nodes in the x-direction and 45 nodes in the y-direction, giving a node size of 4 mm in both directions. The energy balance for any node in Fig. 1 is

$$\tau \frac{dT_i(t)}{dt} = Q_L(t) + Q_R(t) + Q_T(t) + Q_B(t) + Q_{gen}(t) \tag{1}$$

where τ is the thermal mass (J/K), T_i is the node temperature (K), Q_L, Q_R, Q_T, and Q_B are heat conduction or convection terms (W) from the left, right, top, and bottom nodes with respect to node *i*, respectively, and Q_{gen} is the node heat generation (W) at node *i*. The thermal mass is

$$\tau = \rho_{eff} c_{p,eff} V_{cell} \tag{2}$$

where ρ_{eff} is the cell effective density (kg/m^3), $c_{p,eff}$ is the cell effective specific heat capacity (J/kg·K), and V_{cell} is the cell volume. This work takes an effective thermal property approach, thereby reducing the composite battery cell to a pseudo material with effective thermal properties. The material and thermal properties of all layers of a lithium ion cell with a $LiCoO_2$ positive electrode composition and a Li_xC_6 negative electrode composition are given in Table I [16-18].

TABLE I
Material and thermal properties for all layers of a lithium ion cell with a $LiCoO_2$ positive electrode composition and a Li_xC_6 negative electrode composition

	$x(\mu m)$	$\rho(kg/m^3)$	$c_p(J/kg\times K)$	$k_t(W/m\times K)$
Cathode	80	2328	1269	1.58
Anode	88	1347	1437	1.04
Separator	30	726	1978	0.334
Aluminum Current Collector	14	2702	903	238
Copper Current Collector	14	8933	385	398

The cell dimensions used in this work are 8 x 180 x 150 mm (thickness x height x width); therefore, this cell contains 36 electrode sandwiches. The material properties in Table I are used to determine the effective thermal properties as follows. The cell effective density (kg/m^3) is

$$\rho_{eff} = \frac{m_{cell}}{V_{cell}} \tag{3}$$

where m_{cell} is the cell total mass (kg) and V_{cell} is the cell total volume (m^3). The cell mass is 0.78 kg; therefore, the cell effective density is 3551 kg/m^3. The effective specific heat capacity (J/kg·K) is [16]

$$c_{p,eff} = \frac{\sum \left(\rho c_p\right)_i x_i}{\sum \left(\rho x\right)_i} \tag{4}$$

where *i* refers to the layer and x_i is the i^{th} layer thickness (m). The effective specific heat capacity is 1087 J/kg·K. The battery is typically modeled as a uniform layer with anisotropic thermal conductivity [16]. Therefore, the thermal conductivity along the cell thickness is different than the thermal conductivity along the cell width and height. The battery material thermal conductivities are calculated based on the material porosity and on the fact that the materials are immersed in electrolyte. The material thermal conductivity (W/m·K) with electrolyte is [19]

$$k_{we} = k_{woe}\left(1-\varepsilon\right) + \varepsilon k_e \tag{5}$$

where k_{woe} is the material thermal conductivity without electrolyte (W/m·K), ε is the material porosity, and k_e is the electrolyte thermal conductivity (W/m·K). The thickness ratio is

$$\delta_i = \frac{n x_i}{x_{cell}} \tag{6}$$

where n is the number of electrode sandwiches and x_{cell} is the cell thickness (m). Table II gives the parameters required to determine the cathode, anode, and separator thermal conductivities with electrolyte [19].

TABLE II
Battery cell layer porosity, thickness ratio, and thermal conductivities with electrolyte

	Cathode	Anode	Separator	Al Current Collector	Cu Current Collector
ε	0.385	0.485	0.47	-	-
δ	0.354	0.389	0.133	6.19×10^{-2}	6.19×10^{-2}
$k_e \left(W/m \times K\right)$	0.59	0.59	0.59	-	-
$k_{we} \left(W/m \times K\right)$	1.20	0.822	0.454	238	398

The thermal conductivity (W/m·K) along the cell thickness (x-direction) and the thermal conductivity (W/m·K) along the cell height (y-direction), respectively, are [19]

$$k_x = \frac{1}{\frac{\delta_c}{k_c} + \frac{\delta_a}{k_a} + \frac{\delta_s}{k_s} + \frac{\delta_{acc}}{k_{acc}} + \frac{\delta_{ccc}}{k_{ccc}}} \tag{7}$$

$$k_y = \frac{k_c x_c + k_a x_a + k_s x_s + k_{acc} x_{acc} + k_{ccc} x_{ccc}}{x_{cell}} \tag{8}$$

The abbreviations for the cathode, anode, separator, aluminum current collector, and copper current collector, respectively, are c, a, s, acc, and ccc. Equations (7) and (8) yield k_x = 0.942 W/m·K and k_y = 1.12 W/m·K, respectively. Anisotropic cell characteristics promote the need to use separate heat transfer terms for the x and y-directions. The heat transfer in the horizontal direction from the left and right, respectively, are

$$Q_L(t) = U_h A\left(T_L(t) - T_i(t)\right) \tag{9}$$

$$Q_R(t) = U_h A\left(T_R(t) - T_i(t)\right) \tag{10}$$

where U_h is the horizontal overall heat transfer coefficient (W/m^2·K) between the neighboring node and the node of interest, A is the contact area (m^2), T_L is the temperature (K) from the left and T_R is the temperature (K) from the right. If the node is subjected to environmental temperature from the left or right, $T_L(t) = T_{env}$ or $T_R(t) = T_{env}$, respectively, where T_{env} is the environmental temperature (K). The horizontal overall heat transfer coefficient for a node subjected to conduction from either side is

$$U_h = \frac{1}{\frac{\Delta x}{k_x} + \frac{\Delta x}{k_x}} \tag{11}$$

where Δx is the horizontal thickness of the node under consideration (m). For a node subjected to convection from either side, the overall heat transfer coefficient is

$$U_h = \frac{1}{\frac{\Delta x}{k_x} + \frac{1}{h}} \tag{12}$$

where h is the convection heat transfer coefficient (W/m^2·K). The heat transfer from the top and bottom, respectively, are

$$Q_T(t) = U_v A\left(T_T(t) - T_i(t)\right) \tag{13}$$

$$Q_B(t) = U_v A\left(T_B(t) - T_i(t)\right) \tag{14}$$

where U_v is the vertical overall heat transfer coefficient (W/m^2·K) between the neighboring node and the node of interest, T_T is the temperature (K) from the top, and T_B is the temperature (K) from the bottom. If the node is subjected to environmental temperature from the top or bottom, $T_T(t) = T_{env}$ or $T_B(t) = T_{env}$, respectively. The

vertical overall heat transfer coefficients for a node subjected to conduction from the top or bottom is

$$U_v = \frac{1}{\frac{\Delta y}{k_y} + \frac{\Delta y}{k_y}} \tag{15}$$

where Δy is the node vertical thickness (m). For a node subjected to convection from the top or bottom, the overall heat transfer coefficient is

$$U_v = \frac{1}{\frac{\Delta y}{k_y} + \frac{1}{h}} \tag{16}$$

The heat generation in this model is determined using a single particle approach. The governing equation for the i^{th} node heat generation is [9]

$$Q_{gen}(t) = a_n j_{app}\left(T_i\left(\frac{\partial U_n(t)}{\partial T} - \frac{\partial U_p(t)}{\partial T}\right) + U_p(t) - U_n(t) - V_i(t)\right) \tag{17}$$

where a_n is the node area (m^2), j_{app} is the applied current density (A/m^2), $\frac{\partial U_n}{\partial T}$ is the derivative of the anode open circuit potential with respect to temperature (V/K), $\frac{\partial U_p}{\partial T}$ is the derivative of the cathode open circuit potential with respect to temperature (V/K), U_p is the cathode open circuit potential (OCP) (V), U_n is the anode OCP (V), and V_i is the potential of the i^{th} node (V). All time varying parameters in equation (17) are determined using an electrochemical single particle model. Details of this model can be found in Appendix A. Note that the single particle model is valid up to only 1C rate for high-power cells. The single particle model fails for high currents because the concentration profiles in the electrodes are no longer uniform. The deviation is expected since the

single particle model is based on the assumption that currents are small and the electrolyte conductivity is large enough to avoid accumulation of concentration gradients [20]. For this reason, all of the simulations in this paper are conducted at a 1C discharge rate. Fig. 2 depicts the heat generation values for a 1C discharge rate using the single particle model. The current density is a constant 30 A/m^2.

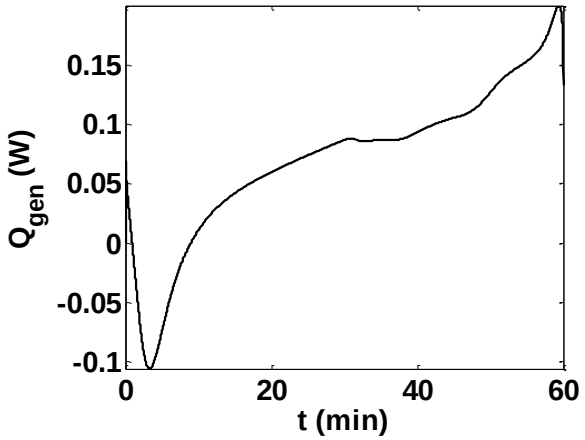

Fig. 2. Node heat generation for a 1C discharge rate and j_{app} = 30 A/m^2.

Notice that from 2-10 minutes in the 1C discharge pictured in Fig. 2, the chemical reaction in the cell is endothermic; thus, causing the heat generation to be negative. Experimental data validating the endothermic effects can be found in Section 2, Appendix A.

Combining equations (1)-(17) into a numerical simulation using the Runge-Kutta 4th order algorithm yields the temperature profile results shown in Fig. 3. The initial temperature for all nodes is 25°C and the battery is subjected to natural convection. The environment is set at a constant 25°C with a 10 W/m^2·K convection heat transfer coefficient. The simulation timestep is 1 s. Fig. 3 shows the time history of the maximum and minimum temperature profiles in the cell, demonstrating that the temperature gradient generated in the prismatic cell is 2°C.

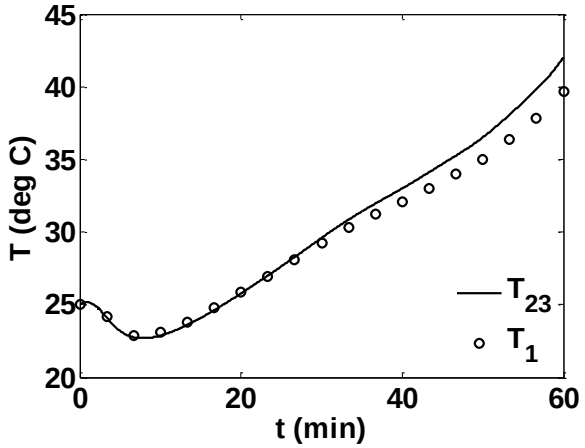

Fig. 3. Temperature profiles of nodes 1 and 23 for battery cell shown in Fig. 1 with heat generation, natural convection, and T_{env} = 25°C.

The maximum temperature in the cell is 42°C. Lithium ion battery cells have specific operating temperature ranges; typically, between -10 and 50°C [1]. Fig. 3 shows that a cell exposed to an environmental temperature of 25°C will remain within the recommended temperature range. In Fig. 4 the lithium ion battery cell is exposed to environmental temperatures of 25, 35, and 45°C.

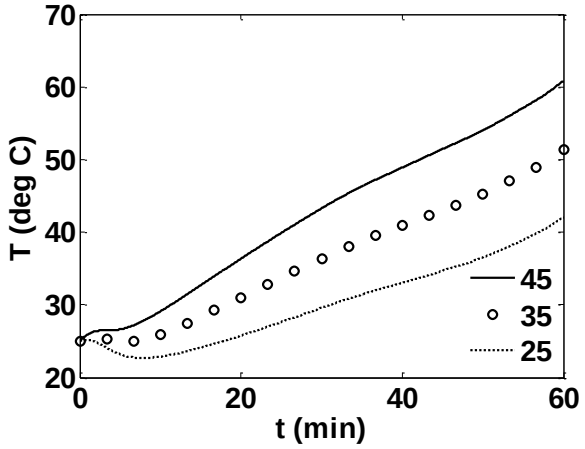

Fig. 4. Temperature profiles of node 23 for battery cell shown in Fig. 1 with heat generation, natural convection, and T_{env} = 25, 35, and 45°C.

A lithium ion cell exposed to an environmental temperature of 35°C eventually reaches 52°C at the end of the 1C discharge cycle, while a cell exposed to an environmental temperature of 45°C surpasses 60°C after discharging for 60 min. Rapid deterioration of battery active material may occur at temperatures over 60°C [21]. Results from Fig. 4 show that cooling is necessary depending on the battery application and the operating environment. Furthermore, higher C-rate discharges will cause even higher cell temperatures than portrayed in Fig. 4.

III. CONVECTION MODEL

This section will detail the addition of a fluid channel to the bottom of the cell with the intention of reducing the maximum cell temperature. The fluid mass flow rate and fluid temperature are controllable inputs into the system. Fig. 5 shows a schematic of a cell with a fluid channel and aluminum heat sink.

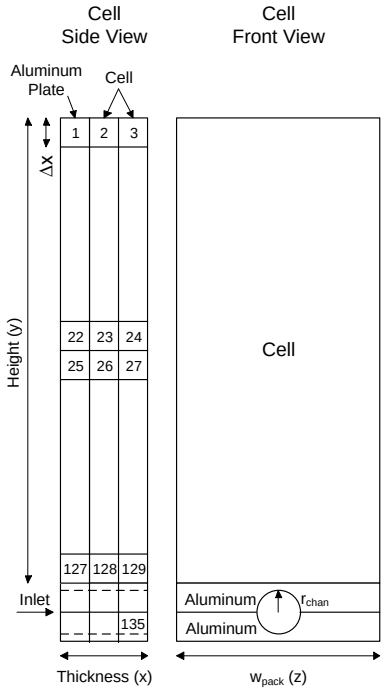

Fig. 5. Cell schematic with fluid channel on bottom and aluminum heat sink on left side.

In this model two different materials (aluminum and cell aluminum casing) are mated at a specified pressure and temperature. Thus, thermal contact resistance must be taken into account. Although neglected in many heat transfer models, thermal contact resistance plays an important role in composite systems where the temperature gradient across the interface between materials may be substantial [22]. The heat transfer equations for the cell bottom nodes are modified and additional differential equations are added to describe the heat transfer in the fluid channel. At these locations (nodes 128 and 129 shown in Fig. 5) the heat transfer from the top and bottom, respectively, are

$$Q_T(t) = \frac{1}{R_c}\left(T_T(t) - T_i(t)\right) \tag{18}$$

$$Q_B(t) = \frac{1}{R_c}\left(T_B(t) - T_i(t)\right) \tag{19}$$

where R_c is the contact resistance (K/W). The contact resistance is

$$R_c = \frac{R_{tc}^{"}}{A_{alp \to cell}} \tag{20}$$

where $R_{tc}^{"}$ is the thermal contact resistance ($m^2 \cdot K/W$) and $A_{alp \to cell}$ is the aluminum plate to cell contact area (m^2). The thermal contact resistance is taken to be 1.5×10^{-4} $m^2 \cdot K/W$, which is the experimental value for an aluminum/aluminum contact [22]. The aluminum plate to cell contact area is

$$A_{alp \to cell} = w_{alp} \Delta x \tag{21}$$

where w_{alp} is the aluminum plate width (m).

The energy balance for the fluid channel is

$$\tau \frac{dT_i(t)}{dt} = Q_L(t) + Q_R(t) + Q_T(t) + Q_B(t) + Q_{fl}(t) \tag{22}$$

where Q_{fl}, the heat transfer from the fluid, is

$$Q_{fl}(t) = h_{fl} A_{wet} \left(T_{fl} - T_i(t) \right) \tag{23}$$

and h_{fl} is the fluid convective heat transfer coefficient ($W/m^2 \cdot K$), A_{wet} is the wetted area (m^2), and T_{fl} is the fluid temperature (K). A ten cell simulation was conducted using ANSYS CFX and it was determined that the temperature gradient from the fluid channel inlet to outlet was only 1.5°C (refer to Section 2, Appendix B). Therefore, the fluid temperature gradient is neglected in this model and the fluid temperature is assumed to be a constant. The wetted area is

$$A_{wet} = \pi r_{chan} \Delta x \tag{24}$$

where r_{chan} is the fluid channel radius (m). The heat transfer from the left and right can be described using equations (9)-(12), with the exception of the area term. For the cells subjected to conduction or convection in the horizontal direction of the channel, the area term in equations (9) and (10) is replaced with

$$A = \left(w_{alp} \Delta x \right) - \frac{\pi}{2} r_{chan}^2 \tag{25}$$

The fluid convective heat transfer coefficient is determined as follows. The type of flow is determined by the Reynolds number

$$\mathrm{Re}_D = \frac{4\dot{m}}{\pi D \mu} \tag{26}$$

where $\dot{m}$ is the fluid mass flow rate (kg/s), D is the channel diameter (m), and μ is the viscosity (kg/m·s). Refer to Table III for the Reynolds numbers used in this work. The Reynolds number ranges from 703-3559; therefore, the flow is laminar for low mass flow rates and turbulent for high mass flow rates (i.e., $\mathrm{Re}_D \geq 2300$). If the flow is laminar and fully developed

$$\frac{L}{D} \geq 5\mathrm{x}10^{-2}\, \mathrm{Re}_D\, \mathrm{Pr} \tag{27}$$

where L is the channel length (m) and Pr is the Prandtl number. Refer to Table III for the Prandtl numbers used in this work. If the flow is turbulent and

$$\frac{L}{D} \geq 10 \tag{28}$$

the flow is fully developed. Due to the short channel length, 12×10^{-3} m, the flow in this work is always developing. Since the flow is developing in the channel, the Nusselt number is

$$\mathrm{Nu}_D = 3.39 + \frac{6.68\mathrm{x}10^{-2}\left(\frac{D}{L}\right)\mathrm{Re}_D\,\mathrm{Pr}}{1+4\mathrm{x}10^{-2}\left[\left(\frac{D}{L}\right)\mathrm{Re}_D\,\mathrm{Pr}\right]^{\frac{2}{3}}} \tag{29}$$

Therefore, the fluid convective heat transfer coefficient is

$$h_{fl} = \frac{k_{fl}\mathrm{Nu}_D}{D} \tag{30}$$

where k_{fl} is the fluid conductivity (W/m·K). All properties of water can be found in [20]. The fluid convection coefficient is determined over a range of applicable mass flow rates for this application and can be seen in Fig. 6. Fig. 6 gives results for a fluid temperature of 25°C.

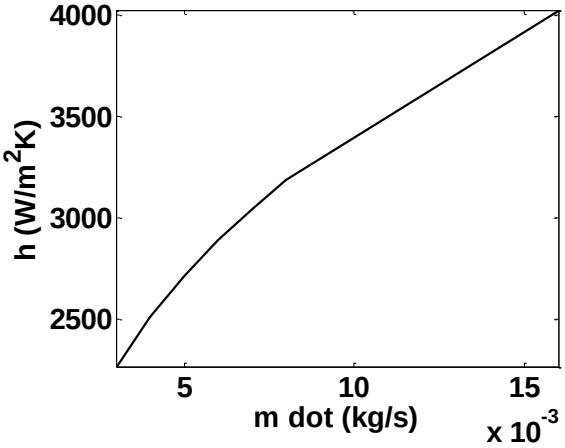

Fig. 6. Fluid convection coefficients for range of applicable mass flow rates and T_{fl} = 25°C.

Table 3 gives the Reynolds numbers, fluid convection coefficients, and Prandtl numbers of water for varying fluid temperatures and mass flow rates.

TABLE III
Reynolds numbers, Prandtl numbers, and fluid convection coefficients for different fluid temperatures and different mass flow rates

$T_{fl}\,(°C)$	**5**	**10**	**15**	**20**	**25**
$\dot{m}\,(kg/s)$			Re_D		
5	703	817	936	1055	1186
10	1406	1634	1873	2100	2373
15	2109	2452	2809	3166	3559
$\dot{m}\,(kg/s)$			$h_{fl}\,(W/m^2 \times K)$		
5	2624	2647	2669	2684	2707
10	3321	3350	3379	3399	3428
15	3799	3833	3866	3889	3922
			Pr		
	11	9.35	8.03	6.97	6.13

The initial temperatures of all of the nodes in the following numerical simulation studies are 25°C. The heat generation in Fig. 2 is a time varying input at each node. The inputs are the environmental natural convection, the fluid temperature, and the fluid convective heat transfer coefficient, which is a function of the fluid mass flow rate. The simulation timestep is 0.1 s. Fig. 7 depicts results for a simulation of the hottest spot in the battery (node 12) with varying fluid temperatures of 5, 15, and 25°C when a cell is subjected to a 45°C environmental temperature. The mass flow rate is 5×10^{-3} kg/s.

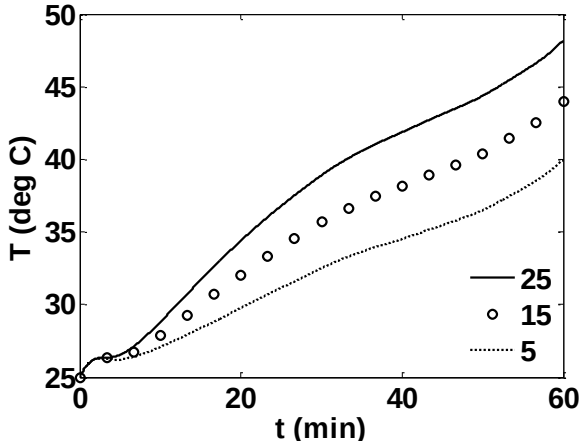

Fig. 7. Temperature profiles of node 12 for battery cell in Fig. 5 with heat generation, forced and natural convection, T_{fl} = 5, 15, and 25°C, T_{env} = 45°C, and $\dot{m} = 5 \times 10^{-3}$ kg/s.

Fig. 7 reveals that all fluid temperatures are successful in substantially reducing the maximum cell temperature within the suggested lithium ion cell operating temperature range. Fluid temperatures of 5, 15, and 25°C yield temperatures at the end of a 1C discharge of 40, 44, and 48°C, respectively. Fig. 8 depicts the effect of different mass flow rates on the temperature profile. The environmental temperature is 45°C, $T_{fl} = 25°\text{C}$, and $\dot{m} = 5 \text{ x } 10^{-3}, 10 \text{ x } 10^{-3}, \text{ and } 15 \text{ x } 10^{-3}$ kg/s.

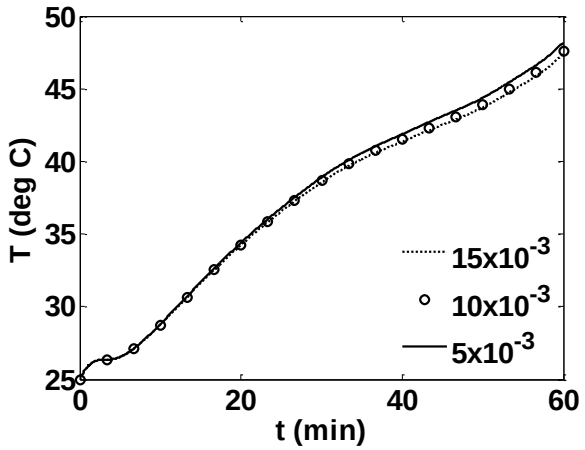

Fig. 8. Temperature profiles of node 12 for battery cell shown in Fig. 5 with heat generation, forced and natural convection, T_{fl} = 25°C, T_{env} = 25°C, and $\dot{m} = 15\times10^{-3},\ 10\times10^{-3},$ and 5×10^{-3} kg/s .

Fig. 8 shows that all mass flow rates allow the lithium ion cell to remain within the specified temperature range. Mass flow rates of 15 x 10^{-3}, 10 x 10^{-3}, and 5 x 10^{-3} kg/s all yield temperatures around 47°C at the end of a 1C discharge. Note that for the range of fluid mass flow rates considered for this application, the effect of the fluid mass flow rate change on the battery temperature is minimal. Comparing Fig. 7 and 8, it is apparent that adjusting the fluid temperature is more effective than adjusting the fluid mass flow rate. Therefore, this work will use a constant mass flow rate of 10 x 10^{-3} kg/s. A system efficiency analysis was conducted (refer to Section 2, Appendix C).

For control design, the order of the model is of concern. The models proposed in the sections entitled "Single Cell Thermal Model" and "Convection Model" contain 90 and 135 nodes, respectively; therefore, their model orders are 90 and 135, respectively. Consequently, the proposed models are not appropriate for control design. The following sections will detail the process of reducing a high order battery model into a small set of differential equations, amendable to controller design.

IV. MODEL ORDER REDUCTION

Linearization and Model Order Reduction (MOR) of the previous cell temperature model is necessary in order to apply control theory. Very detailed models have been described in previous sections that capture the dynamics of the lithium ion battery temperature profile during discharge. The goal of this section is to capture those dynamics while making the model more applicable to control design. The Global Arnoldi Algorithm (GAA) [15] is used to reduce high order non-linear MIMO systems into a substantially lower order set of equations. Typically, the algorithm is applied to linearized or weakly non-linear systems [14]. Therefore, in order to proceed with the GAA, the system is linearized about an equilibrium temperature trajectory. The linearization and MOR results will be described in detail for node 12 in Fig. 5. This node produces the maximum temperature in the cell and this work is conducted under the assumption that a controller will be designed based on the maximum cell temperature.

The set of temperature differential equations can be described in the state space form

$$\mathbf{f} = \dot{\mathbf{T}}(t) = g\left(\mathbf{T}(t)\right) + \mathbf{C}\mathbf{u}(t) \tag{31}$$

where $\mathbf{T}$ is the n x 1 state vector of node temperatures, $\mathbf{C}$ is the n x n Jacobian input matrix, and $\mathbf{u}$ is the n x 1 input vector. The equilibrium state trajectory vector is

$$\bar{\mathbf{T}}(t) = \left[\bar{T}_1(t) \ \cdots\cdots \ \bar{T}_n(t)\right]^T \tag{32}$$

where each vector element is an m^{th} order polynomial. The equilibrium input vector is

$$\bar{\mathbf{u}} = \left[\bar{u}_1 \ \cdots\cdots \ \bar{u}_n\right]^T \tag{33}$$

In this paper, the equilibrium input vector is composed of constant environmental temperature inputs or constant fluid temperature inputs. The vector of perturbation states is

$$\hat{\mathbf{T}}(t) = \mathbf{T}(t) - \bar{\mathbf{T}}(t) = \left[\hat{T}_1(t) \ \cdots\cdots \ \hat{T}_n(t) \right]^T \tag{34}$$

Performing a Taylor series expansion for the first node, where the second order and higher order terms are neglected

$$\dot{T}_1(t) \approx f_1\left(\bar{\mathbf{T}}, \bar{\mathbf{u}}, t\right) + \left.\frac{\partial f_1}{\partial T_1}\right|_{\bar{T}_1, \bar{u}_1} \hat{T}_1 + \cdots + \left.\frac{\partial f_1}{\partial T_n}\right|_{\bar{T}_n, \bar{u}_n} \hat{T}_n + \left.\frac{\partial f_1}{\partial u_1}\right|_{\bar{T}_1, \bar{u}_1} \hat{u} + \cdots \left.\frac{\partial f_1}{\partial u_n}\right|_{\bar{T}_n, \bar{u}_n} \hat{u}_n \tag{35}$$

The linearized dynamics are

$$\dot{\hat{\mathbf{T}}}(t) = \mathbf{J}_T \hat{\mathbf{T}}(t) + \mathbf{J}_u \hat{\mathbf{u}}(t) \tag{36}$$

where the perturbation input vector is

$$\hat{\mathbf{u}}(t) = \mathbf{u}(t) - \bar{\mathbf{u}} = \left[\hat{u}_1 \ \cdots\cdots \ \hat{u}_n \right]^T \tag{37}$$

and the Jacobian matrices are

$$\mathbf{J}_T = \left[\begin{matrix} \frac{\partial f_1}{\partial T_1} & \cdots & \frac{\partial f_1}{\partial T_n} \\ \vdots & \ddots & \vdots \\ \frac{\partial f_n}{\partial T_1} & \cdots & \frac{\partial f_n}{\partial T_n} \end{matrix} \right]_{\bar{\mathbf{T}}, \bar{\mathbf{u}}} \qquad \mathbf{J}_u = \left[\begin{matrix} \frac{\partial f_1}{\partial u_1} & \cdots & \frac{\partial f_1}{\partial u_n} \\ \vdots & \ddots & \vdots \\ \frac{\partial f_n}{\partial u_1} & \cdots & \frac{\partial f_n}{\partial u_n} \end{matrix} \right]_{\bar{\mathbf{T}}, \bar{\mathbf{u}}} \tag{38}$$

The GAA is applied to the system given in equation (36). Conceptually, given $\mathbf{A},\mathbf{B}\in\mathbb{R}^{n\,x\,n}$, the GAA yields $\mathbf{A}_R\in\mathbb{R}^{q\,x\,q}$ and $\mathbf{B}_R\in\mathbb{R}^{q\,x\,n}$, where $q\ll n$ (q is desired model order). In the GAA, the input matrix $\mathbf{B}$ is treated as a stacked vector. Therefore, the matrix $\mathbf{A}$ is

$$\mathbf{A}=\left(\mathbf{I}_s\otimes\left(\mathbf{J}_T\right)^q\right) \tag{39}$$

where $\mathbf{I}_s$ is the *s* x *s* identity matrix (*s* is the number of inputs, *s* = *n* in this work) and $\otimes$ denotes the Kronecker product. The matrix $\mathbf{B}$ is

$$\mathbf{B}=vec\left(\mathbf{J}_u\right) \tag{40}$$

where the *vec* operator is a stacking operation (i.e., the matrix columns are stacked on one another). The pair inserted into the GAA is $\left(\left(\mathbf{I}_s\otimes\left(\mathbf{J}_T\right)^q\right),vec\left(\mathbf{J}_u\right)\right)$. The GAA will recursively generate the Frobenius orthonormal basis

$$\Psi_q=\left[\mathbf{V}_1\ \cdots\cdots\ \mathbf{V}_q\right] \tag{41}$$

from the matrix Krylov subspace

$$K_q\left(\mathbf{A},\mathbf{B}\right)=\text{span}\left\{\mathbf{B},\mathbf{AB},\ \cdots,\mathbf{A}^{q-1}\mathbf{B}\right\} \tag{42}$$

where q is the desired system order. The Krylov subspace has the properties

$$\left\langle\mathbf{V}_i,\mathbf{V}_j\right\rangle_F=0\text{ for }i\neq j;\ i,j=0,1,\cdots,q-1 \tag{43}$$

$$\left\langle\mathbf{V}_i,\mathbf{V}_j\right\rangle_F=1\text{ for }i=j \tag{44}$$

where the subscript F denotes the Frobenius norm

$$\left\langle \mathbf{V}_i, \mathbf{V}_j \right\rangle_F = \text{trace}\left(\mathbf{A}^T\mathbf{B}\right) \tag{45}$$

A more detailed description of the GAA [15] follows by first setting

$$\mathbf{V}_1 = \frac{\mathbf{B}}{\|\mathbf{B}\|_F} \tag{46}$$

Subsequently, $\mathbf{V}_1$ becomes the first element in the matrix

$$\Psi_q = \left[\mathbf{V}_1\right] \tag{47}$$

Moreover, setting

$$\mathbf{V}' = \mathbf{B}\mathbf{V}_1 \tag{48}$$

the elements of

$$\mathbf{h} = \left\langle \mathbf{V}_1, \mathbf{V}' \right\rangle_F = trace\left(\mathbf{V}_1^T\mathbf{V}'\right) \tag{49}$$

$$\mathbf{V}' = \mathbf{A}\mathbf{V}_1 - \mathbf{V}_1\mathbf{h} \ \perp \ \mathbf{V}_1 \tag{50}$$

are recursively determined until $i = q$. The final value from equation (50) is used to determine

$$\mathbf{h}\left(j+1, j\right) = \left\|\mathbf{V}'\right\|_F \tag{51}$$

and

$$\mathbf{V}(j+1) = \frac{\mathbf{V}'}{\mathbf{h}(j+1, j)} \tag{52}$$

$$\Psi = \begin{bmatrix} \mathbf{V}_q & \cdots & \mathbf{V}_{q+1} \end{bmatrix} \tag{53}$$

Equations (46)-(52) are then recursively completed until $j = q$. The reduced system is [15]

$$\mathbf{A}_R = \Psi^+ \mathbf{A} \Psi \tag{54}$$

$$\mathbf{B}_R = \Psi^+ \mathbf{B} \tag{55}$$

where

$$\Psi^+ = \left(\Psi^T \Psi\right)^{-1} \Psi^T \tag{56}$$

For a first order reduction of the system pictured in Fig. 5 the matrices $\mathbf{A}_R$ (q x q) and $\mathbf{B}_R$ (1 x n) are

$$\mathbf{A}_R = \begin{bmatrix} -3.7334 \end{bmatrix} \tag{57}$$

$$\mathbf{B}_R = \begin{bmatrix} -3.2\times10^{-3} & 1.1\times10^{-3} & 0 & 7.7\times10^{-3} & 0 & \cdots & \cdots & 0 \end{bmatrix} \tag{58}$$

V. RESULTS

The results of linearization and the GAA are analyzed for a single lithium ion cell with natural and forced convection (Fig. 5). Linearization of each node is conducted using equilibrium trajectories obtained by a polynomial curve fit. Fig. 9 shows the linearization results using second, third, and fourth order polynomial equilibrium trajectories. The simulation is conducted with an environmental temperature of 35°C, mass flow rate of 10 x 10^{-3} kg/s, and a fluid temperature of 15°C. Note that all of the

following simulation results are for a 1C discharge rate and the node with the maximum temperature at the end of the 1C discharge (node 12 in Fig. 5).

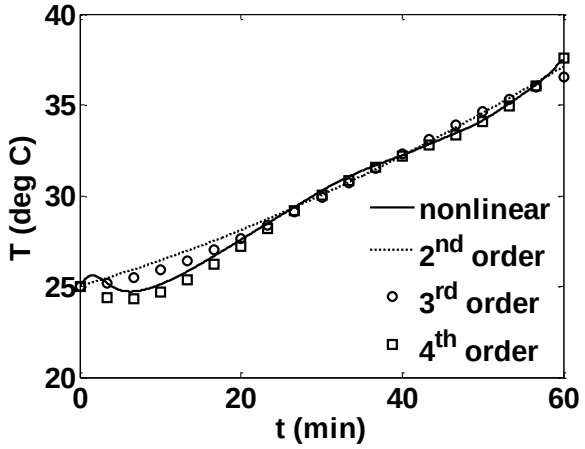

Fig. 9. Non-linear and linearization maximum cell temperature profiles using second, third, and fourth order polynomial equilibrium trajectories with T_{fl} = 15°C, T_{env} = 35°C, and $\dot{m} = 10 \times 10^{-3}$ kg/s .

Table IV shows the average percent difference between the non-linear temperature profile and linearization with various order equilibrium trajectories. Results in Table IV illustrate an increase in accuracy as the polynomial order increases. Results show that linearization with any order trajectory will result in an average percent difference no higher than 2.09%. For a fourth order polynomial and higher, the difference between the non-linear and linear temperature profiles remains below 1%. A fourth order equilibrium trajectory is used for all simulation studies in this work.

TABLE IV
Average percent difference between linearized and non-linear temperature profiles for different equilibrium trajectory orders

Equilibrium Trajectory Order	Average Percent Difference (%)
1	2.09
2	1.62
3	1.24
4	0.95
5	0.95
6	0.93
7	0.89

As discussed earlier, the inputs into this system are the fluid temperature and the environmental temperature. Consequently, for this model to be control oriented the coefficients of the fourth order polynomial must be described as a function of the environmental and fluid temperature. The environmental and fluid temperature ranges are 25-45°C and 25-5°C, respectively.

In order to define the equilibrium trajectory coefficients as functions of environmental and fluid temperature, twenty five cases are developed by pairing each fluid temperature, $T_{fl} = 25,\ 20,\ 15,\ 10,\ 5°\mathrm{C}$, with each environmental temperature, $T_{env} = 25,\ 30,\ 35,\ 40,\ 45°\mathrm{C}$. Fourth order equilibrium trajectories for each case are of the form

$$\bar{T}(t) = at^4 + bt^3 + ct^2 + dt + e \tag{59}$$

The coefficients are computed using the linear regression function in the MATLAB surface fitting toolbox for models of the form

$$a\left(T_{env}, T_{fl}\right) = a_0 + a_1 T_{env} + a_2 T_{fl} \tag{60}$$

Table V provides the coefficients in equation (60) for each coefficient in equation (59) and the respective R-squared values. The 0, 1, and 2 refer to the coefficient subscripts in equation (60). Note that the values in Table V are poorly scaled. This can be rectified by changing the time scale to minutes or hours. The coefficients can now be described as functions of environmental and fluid temperature; therefore, linearization about an equilibrium trajectory can be completed for any combination of environmental and fluid temperatures.

TABLE V
Coefficients in equation (60) and respective correlation coefficients, determined using linear regression function in MATLAB surface fitting toolbox

Coefficient	**0**	**1**	**2**	$\mathbf{R^2}$
a (K/s^4)	-1.56×10^{-12}	-3.81×10^{-15}	1.11×10^{-14}	1
b (K/s^3)	4.13×10^{-9}	4.80×10^{-11}	-7.83×10^{-11}	1
c (K/s^2)	4.54×10^{-5}	-2.37×10^{-7}	1.29×10^{-7}	1
d (K/s)	-0.228	5.69×10^{-4}	1.65×10^{-4}	1
e (K)	306	1.86×10^{-3}	-2.80×10^{-2}	1

The linearized system must be capable of accurately depicting the temperature profile of the cell when the system is undergoing changes in environmental and fluid temperatures. To demonstrate this ability, a simulation is conducted where the environmental and fluid temperature vary linearly from 25 to 45°C and from 25 to 5°C, respectively, over 60 min. Fig. 11 shows the linearization temperature profile for an equilibrium trajectory for $T_{env} = 35°\text{C}$ and $T_{fl} = 15°\text{C}$.

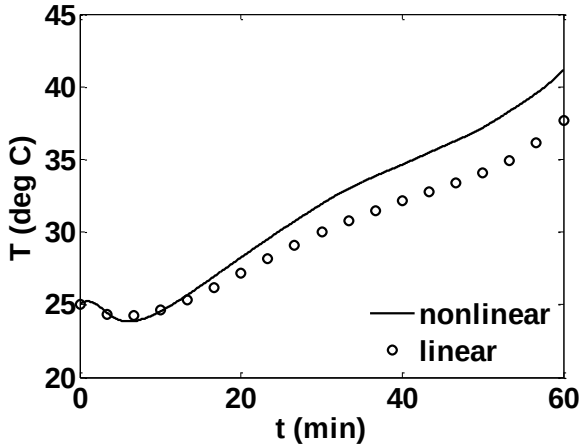

Fig. 10. Non-linear and linearization maximum cell temperature profiles using equilibrium trajectory based on T_{env} = 35°C and T_{fl} = 15°C with linearly varying environmental and fluid temperature from 25-45°C and 25-5°C, respectively.

Fig. 10 demonstrates that the linearized model with equilibrium trajectory based on the mid-range inputs provides a 5.2% difference from the non-linear model. The non-linear temperature profile reaches 41°C, while the linear temperature profile only reaches 38°C, at the end of a 1C discharge. The concept of constant linearization is introduced by allowing the coefficients given by equation (60) to constantly change with environmental and fluid temperatures. Fig. 11 provides results for the same simulation conditions in Fig. 10 but with constant linearization (i.e., the linearization trajectory is updated at each time step).

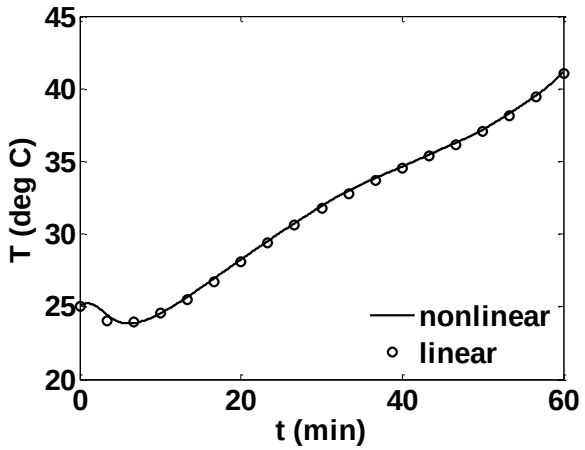

Fig. 11. Non-linear and linearization maximum cell temperature profiles using constant linearization with linearly varying environmental and fluid temperature from 25-45°C and 25-5°C, respectively.

Fig. 11 illustrates very good results between the non-linear system and the constantly linearized system. The average different between the two systems is 0.49%; therefore, constant linearization is used in this work.

Model order reduction must accurately depict the temperature profile of the system when experiencing both static and dynamic inputs. To demonstrate the ability of the GAA to reduce a system with a static input, a simulation with $T_{env} = 35°\text{C}$ and $T_{fl} = 15°\text{C}$ is conducted. The results for model reduction of orders 1 and 3 are shown in Fig. 12. Table VI gives the average percent difference from the non-linear system for model reduction of orders 1-3.

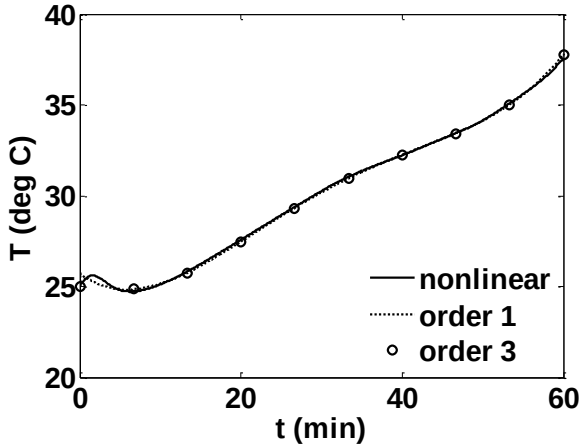

Fig. 12. Non-linear and model reduction of orders 1 and 3 maximum cell temperature profiles with static inputs of T_{env} = 35°C and T_{fl} = 15°C.

TABLE VI
Average percent difference between non-linear system and model reductions of order 1-3

Model Reduction Order	Average Percent Difference (%)
1	0.266
2	0.266
3	0.265

Table VI shows that a first order reduced system provides very good results with a percent difference of 0.266%. Change in model order reduction does not affect the accuracy of the reduced system in comparison with the nonlinear system; therefore, a first order model reduction is used in this work. To demonstrate the predictive capabilities of the reduced model, a simulation is conducted where the environmental and fluid temperature vary linearly from 25 to 45°C and from 25 to 5°C, respectively, over 60 min. The results are shown in Fig. 13.

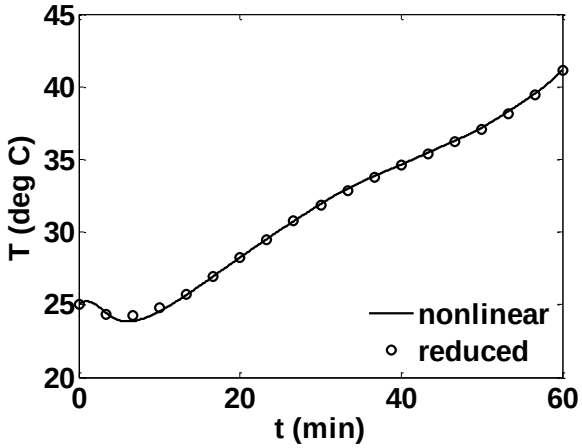

Fig. 13. Non-linear and first order model reduction maximum cell temperature profiles with linearly varying environmental and fluid temperature from 25-45°C and 25-5°C, respectively.

Fig. 13 shows that a first order reduction provides simulation results of a 1C discharge with a 0.35% difference from the non-linear simulation. The results shown in Fig. 13 prove that a first order reduction is capable of accurately reducing a system with varying inputs. The resulting control oriented model can accurately predict the dynamics of a system undergoing input changes; therefore, making it possible to design a thermal controller using this model.

VI. SUMMARY AND CONCLUSIONS

In this work a lithium ion battery cell thermal model was developed through the coupling of a lumped energy balance and a single particle electrochemical heat generation model. If the lithium ion cell is subjected to large environmental temperatures, the cell exceeds the proper operational temperature range during a 1C discharge. Therefore, a cooling channel was added to the bottom of the cell and an aluminum heat sink to the side of the cell. Simulations were conducted for different fluid temperatures and mass flow rates over a wide range of environmental temperatures and it was shown that the cell temperature remains within the desired temperature range when cooling is utilized during

a 1C discharge. Results indicate that changes in fluid temperature have a much greater effect on the cell temperature than changes in mass flow rate. The proposed model is very accurate; however, is not applicable to controller design due to its high order. Therefore, model order reduction techniques were employed to create a control oriented model. Linearization of the non-linear system about different order polynomial equilibrium trajectories was conducted. Linearization with a fourth order polynomial trajectory provides very accurate results with an average percent difference between linear and non-linear simulations of 0.95%; therefore, a fourth order equilibrium trajectory was used throughout this work. Next, functions were derived to relate the equilibrium trajectory coefficients to environmental and fluid temperatures. With these functions, linearization based on an equilibrium trajectory for $T_{env} = 35°\text{C}$ and $T_{fl} = 15°\text{C}$ yielded a 5.2% difference between the linear and non-linear system. The notion of constant linearization, where the linearization trajectory is updated at each timestep based on the current environmental and fluid temperature, was introduced and results yielded a 0.49% difference between the linear and non-linear system. For this reason, constant linearization was used in this work. The system was reduced using the Global Arnoldi Algorithm. A simulation with $T_{env} = 35°\text{C}$ and $T_{fl} = 15°\text{C}$ provided results indicating that the system can be reduced to a first order system with a 0.27% difference between the reduced and non-linear system. The effect of an increase in model reduction order was analyzed and it was determined that it has little effect on the model accuracy; therefore, a first order model reduction was used in this work. A simulation with varying inputs yielded results demonstrating that the system can accurately be reduced to a first order model with a 0.35% difference between the reduced and non-linear model. Therefore, the control oriented model developed in this work is capable of depicting the dynamic behavior of an active liquid cooled lithium ion cell undergoing environmental and fluid temperature changes.

APPENDIX

The following appendix provides the single particle electrochemical model. For more detailed information, the reader may refer to [8, 20, 23]. Empirical relations for the positive (p) and negative (n) electrode derivatives with respect to temperature, respectively, are [8]

$$\frac{\partial U_p(t)}{\partial T} = \frac{-0.19952 + 0.92837y - 1.36455y^2 + 0.61154y^3}{1 - 5.66148y + 11.47636y^2 - 9.82431y^3 + 3.04876y^4} \tag{61}$$

$$\frac{\partial U_n(t)}{\partial T} = \frac{\begin{pmatrix} 5.27\times10^{-3} + 3.29927x - 91.79326x^2 + 1004.91101x^3 \\ -5812.27813x^4 + 19329.7549x^5 - 37147.8947x^6 \\ +38379.18127x^7 - 16515.05308x^8 \end{pmatrix}}{\begin{pmatrix} 1 - 48.09287x + 1017.2348x^2 - 10481.80419x^3 \\ +59431.30001x^4 - 195881.6488x^5 + 374577.3152x^6 \\ -385821.1607x^7 + 165705.8597x^8 \end{pmatrix}} \tag{62}$$

where y is the fraction of lithium ions inserted into Li_yCoO_2 and x is the fraction of lithium ions inserted into Li_xC_6. The fraction of lithium ions inserted into Li_yCoO_2 is

$$y(t) = \frac{c_{s,p}(t)}{c_{s,p}^{\max}} \tag{63}$$

where $c_{s,p}$ is the positive electrode particle surface lithium ion concentration (mol·dm^{-3}) and $c_{s,p}^{\max}$ is the positive electrode intercalation particle maximum lithium ion concentration (mol·dm^{-3}). The fraction of lithium ions inserted into Li_xC_6 is

$$x(t) = \frac{c_{s,n}(t)}{c_{s,n}^{\max}} \tag{64}$$

where $c_{s,n}$ is the negative electrode particle surface lithium ion concentration (mol·dm^{-3}) and $c_{s,n}^{\max}$ is the negative electrode intercalation particle maximum lithium ion concentration (mol·dm^{-3}). The positive or negative electrode particle surface lithium ion concentration is

$$c_{s,i}(t) = m\left(j_{app}, t\right)t + b \tag{65}$$

where i denotes the positive or negative electrode, m is the slope, and b is the y-intercept. Details of determining the positive or negative electrode particle surface lithium ion concentration can be found in [22]. Graphical relationships for the empirical relationships in equations (61) and (62) are given in Fig. 14 and 15, respectively.

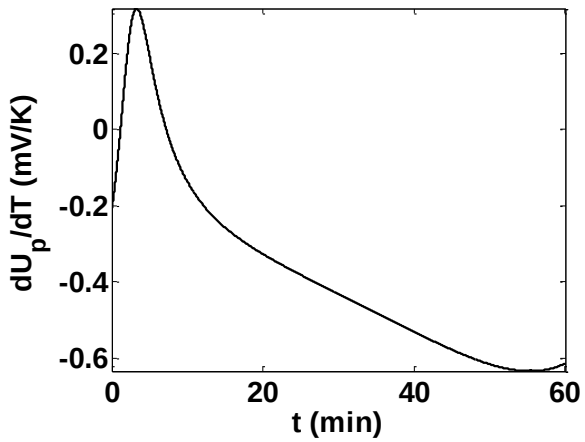

Fig. 14. dU_p/dT time history from equation (61) for a 1C discharge rate.

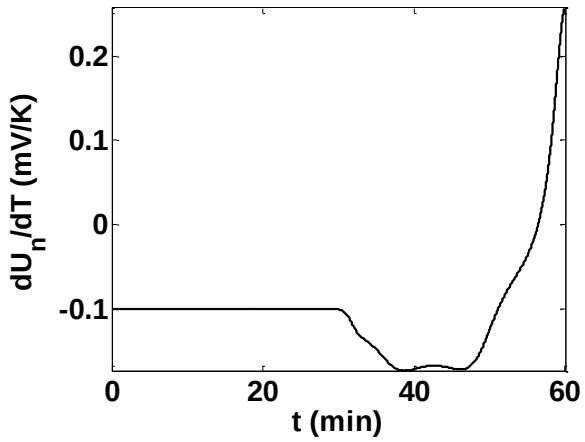

Fig. 15. dU_n/dT time history from equation (62) for a 1C discharge rate.

The anode and cathode open circuit potentials are empirical functions of the concentration of lithium ions in the solid phase obtained by fitting experimental data to polynomial expressions. Empirical relationships for the open circuit potential in the positive electrode (Li_yCoO_2) and negative electrode (Li_xC_6), respectively, are [23]

$$U_p(t) = \frac{-4.656 + 88.669y^2 - 401.119y^4 + 342.909y^6 - 462.471y^8 + 433.434y^{10}}{-1.0 + 18.933y^2 - 79.532y^4 + 37.311y^6 - 73.083y^8 + 95.96y^{10}} \quad (66)$$

$$U_n(t) = 0.7222 + 0.1387x + 0.029x^{0.5} - \frac{0.0172}{x} + \frac{0.0019}{x^{1.5}} + 0.2808e^{(0.90-15x)} - 0.7984e^{(0.4465x-0.4108)} \quad (67)$$

The positive and negative open circuit potentials for a 1C discharge are shown in Fig. 16 and 17, respectively.

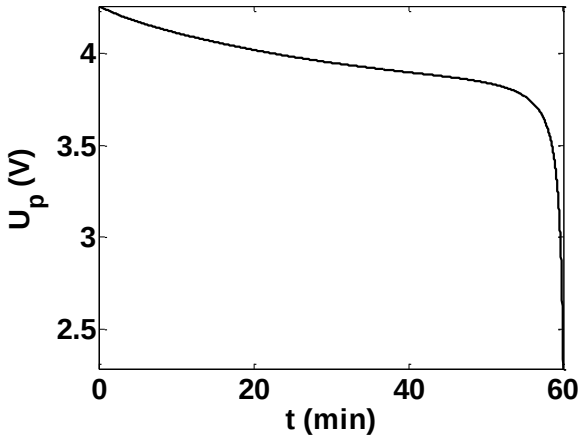

Fig. 16. U_p time history from equation (66) for a 1C discharge rate.

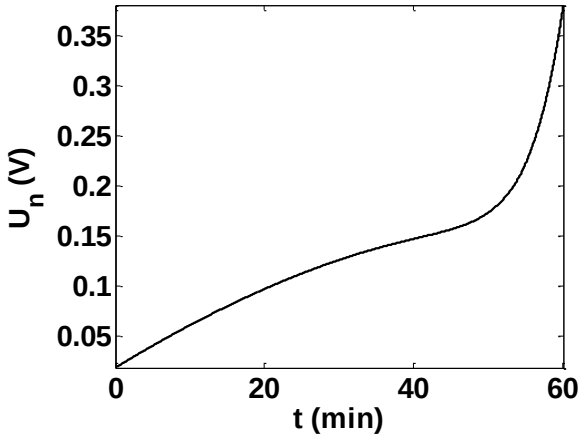

Fig. 17. U_n time history from equation (67) for a 1C discharge rate.

The cell potential is

$$V(t) = \phi_p(t) - \phi_n(t) \tag{68}$$

where ϕ_p and ϕ_n are the solid phase potentials of the positive and negative electrodes, respectively [20]. The solid phase potentials are

$$\phi_i(t) = \sinh^{-1}\left(\frac{j_i^+}{2k_i\sqrt{c_{s,i}^{\max} - c_{s,i}(t)}\sqrt{c_{s,i}(t)c_{s,i}^0}}\right)\cdot\left(\frac{R_i T(t)}{0.5F}\right) + U_i(t) \tag{69}$$

where j_i^+ is the pore wall flux, k_i is the electrochemical reaction rate constant at the positive or negative particle surface ($cm^{-5/2}s^{-1}mol^{-1/2}$), $c_{s,i}^0$ is the initial concentration ($mol \cdot dm^{-3}$), R_i is the positive or negative particle radius (m), and F is Faradays constant (C/mol). The cell potential for the cell used in this paper can be seen in Fig. 18.

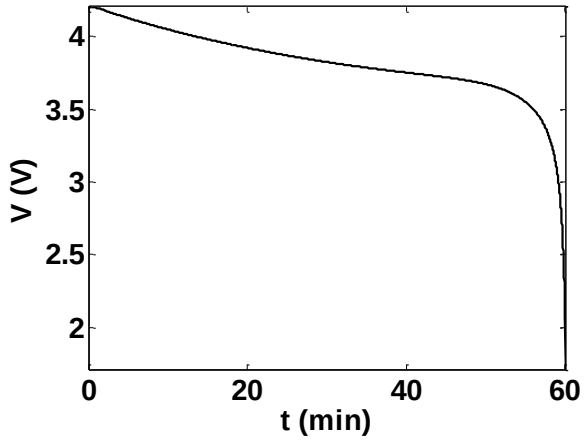

Fig. 18. V time history from equation (68) for a 1C discharge rate.

ACKNOWLEDGMENT

The authors would like to acknowledge the valuable technical discussions with Dr. Kelly Homan.

REFERENCES

[1] C. Mi, B. Li, D. Buck, and N. Ota, "Advanced Electro-Thermal Modeling of Lithium-Ion Battery System for Hybrid Electric Vehicle Applications," *IEEE Vehicle Power and Propulsion Conference*, Arlington, Texas, September 9-12, 2007, pp. 107-111.

[2] X. Zhang, "Multiscale Modeling of Li-Ion Cells: Mechanics, Heat Generation, and Electrochemical Kinetics," Dissertation, The University of Michigan, Department of Mechanical Engineering, 2009.

[3] V. Srinivasan and C.Y. Wang, "Analysis of Electrochemical and Thermal Behavior of Li-Ion Cells," *J. Electrochem. Soc.*, **150** (1), pp. A98-A106, 2003.

[4] W. Fang, O.J. Kwon, and C.Y. Wang, "Electrochemical-Thermal Modeling of Automotive Li-ion Batteries and Experimental Validation Using a Three-Electrode Cell," *Int. J. Energy Res.*, **34**, pp. 107-115, 2010.

[5] W.B. Gu and C.Y. Wang, "Thermal-Electrochemical Modeling of Battery Systems," *J. Electrochem. Soc.*, **147** (8), pp. 2910-2922, 2000.

[6] K.E. Thomas and J. Newman, "Thermal Modeling of Porous Insertion Electrodes," *J. Electrochem. Soc.*, **150** (2), pp. A176-A192, 2003.

[7] D. Bernardi, E. Pawlikowski, and J. Newman, "A General Energy Balance for Battery Systems," *J. Electrochem. Soc.*, **132** (1), pp. 5-12, 1985.

[8] M. Guo, G. Sikha, and R.E. White, "Single-Particle Model for a Lithium-Ion Cell: Thermal Behavior," *J. Electrochem. Soc.*, **158** (2), pp. A122-A132, 2011.

[9] M. Guo and R.E. White, "Thermal Model for Lithium Ion Battery Pack with Mixed Parallel and Series Configuration," *J. Electrochem. Soc.*, **158** (10), pp. A1166-A1176, 2011.

[10] D. Zhang, B.N. Popov, and R.E. White, "Modeling Lithium Intercalation of a Single Spinel Particle Under Potentiodynamic Control," *J. Electrochem. Soc.*, **147** (3), pp. 831-838, 2000.

[11] Y. Ma, H. Teng, and M. Thelliez, "Electro-Thermal Modeling of a Lithium-Ion Battery System," *SAE Int. J. Engines*, **3** (2), pp. 306-317, 2010.

[12] Y. Chen and J.W. Evans, "Heat Transfer Phenomena in Lithium/Polymer-Electrolyte Batteries for Electric Vehicle Application," *J. Electrochem. Soc.*, **140** (7), pp. 1833-1838, 1993.

[13] R. Bartholomaeus, C. Klaucke, and H. Wittig, "Control-Oriented Dynamic Li-Ion Battery Models for High Power Applications," *EVS24 International Battery, Hybrid and Fuel Cell Electric Vehicle Symposium*, Stravanger, Norway, May 13-16, 2009.

[14] J. Chen, S.M. Kang, J. Zou, C. Liu, and J.E. Schutt-Aine, "Reduced-Order Modeling of Weekly Nonlinear MEMS Devices With Taylor-Series Expansion and Arnoldi Approach," *J. Microelectomech. Sys.*, **13** (3), pp. 441-451, 2004.

[15] M.H. Lai, C.C. Chu, and W.S. Feng, "MIMO Interconnects Order Reductions by Using the Global Arnoldi Algorithm," *IEEE International Symposium on Circuits and Systems*, Island of Kos, Greece, May 21-24, 2006, pp. 1107-1110.

[16] T.M. Bandhauer, S. Garimella, and T.F. Fuller, "A Critical Review of Thermal Issues in Lithium-Ion Batteries," *J. Electrochem. Soc.*, **158** (3), pp. R1-R25, 2011.

[17] V.R. Subramanian, V. Boovaragavan, V. Ramadesigan, and M. Arabandi, "Mathematical Model Reformulation for Lithium-Ion Battery Simulations: Galvanostatic Boundary Conditions," *J. Electrochem. Soc.*, **156** (4), pp. A260-A271, 2009.

[18] H. Maleki, S.A. Hallaj, J.R. Selman, R.B. Dinwiddie, and H. Wang, "Thermal Properties of Lithium-Ion Battery and Components," *J. Electrochem. Soc.*, **146** (3), pp. 947-954, 1999.

[19] T. Peng and Z. Hongwei, "Research on Thermo-Physical Properties Identification and Thermal Analysis of EV Li-ion Battery," Beijing Institute of Technology: School of Mechanical and Vehicular Engineering, Beijing, P.R. of China, 2009.

[20] N.A. Chaturvedi, R. Klein, J. Christensen, J. Ahmed, and A. Kojic, "Algorithms for Advanced Battery-Management Systems: Modeling Estimation and Control Challenges for Lithium-Ion Batteries," *IEEE Control Systems Magazine*, **30** (3), pp. 46-68, 2010.

[21] K. Tikhonov and V.R. Kock, "Li-Ion Battery Electrolytes Designed for a Wide Temperature Range," *Covalent Associates, Inc.*, Woburn, MA.

[22] F.P. Incropera, D.P. DeWitt, T.L. Bergman, and A.S. Lavine, "Introduction to Heat Transfer," John Wiley and Sons, Fifth Edition, 2007.

[23] S. Santhanagopalan and R.E. White, "Online Estimation of the State of Charge of a Lithium Ion Cell," *J. Power Sources*, **161**, pp. 1346-1355, 2006.

SECTION

2. CONCLUSIONS

In this work a lithium ion battery cell thermal model was developed through the coupling of a lumped energy balance and a single particle electrochemical heat generation model. If the lithium ion cell is subjected to large environmental temperatures, the cell exceeds the proper operational temperature range during a 1C discharge. Therefore, a cooling channel was added to the bottom of the cell and an aluminum heat sink to the side of the cell. Simulations were conducted for different fluid temperatures and mass flow rates over a wide range of environmental temperatures and it was shown that the cell temperature remains within the desired temperature range when cooling is utilized during a 1C discharge. Results indicate that changes in fluid temperature have a much greater effect on the cell temperature than changes in mass flow rate. The proposed model is very accurate; however, is not applicable to controller design due to its high order. Therefore, model order reduction techniques were employed to create a control oriented model. Linearization of the non-linear system about different order polynomial equilibrium trajectories was conducted. Linearization with a fourth order polynomial trajectory provides very accurate results with an average percent difference between linear and non-linear simulations of 0.95%; therefore, a fourth order equilibrium trajectory was used throughout this work. Next, functions were derived to relate the equilibrium trajectory coefficients to environmental and fluid temperatures. With these functions, linearization based on an equilibrium trajectory for $T_{env} = 35°\text{C}$ and $T_{fl} = 15°\text{C}$ yielded a 5.2% difference between the linear and non-linear system. The notion of constant linearization, where the linearization trajectory is updated at each timestep based on the current environmental and fluid temperature, was introduced and results yielded a 0.49% difference between the linear and non-linear system. For this reason, constant linearization was used in this work. The system was reduced using the Global Arnoldi Algorithm. A simulation with $T_{env} = 35°\text{C}$ and $T_{fl} = 15°\text{C}$ provided results indicating that the system can be reduced to a first order system with a 0.27%

difference between the reduced and non-linear system. The effect of an increase in model reduction order was analyzed and it was determined that it has little effect on the model accuracy; therefore, a first order model reduction was used in this work. A simulation with varying inputs yielded results demonstrating that the system can accurately be reduced to a first order model with a 0.35% difference between the reduced and non-linear model. Therefore, the control oriented model developed in this work is capable of depicting the dynamic behavior of an active liquid cooled lithium ion cell undergoing environmental and fluid temperature changes.

In regards to future work, the control oriented model developed in this work is applicable to controller design. Experimental results will validate the high and low order models developed in this work. An experimental active liquid system must be developed. Thermal controller design and validation must be completed.

APPENDIX A.
EXPERIMENTAL DATA

The following appendix provides experimental data obtained for a 10Ah lithium ion battery ($LiFePO_4$). The battery was discharged using the current profile in Figure 1.

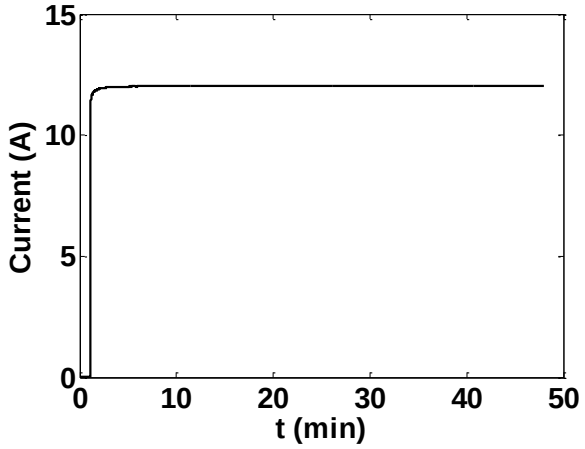

Figure 1. Current profile used to discharge battery.

The temperature was measured using an LM35 Precision Centigrade Temperature Sensor from National Semiconductor. The accuracy of this sensor at 25°C is ±0.5°C. The temperature results for the discharge current profile in Figure 1 are shown in Figure 2.

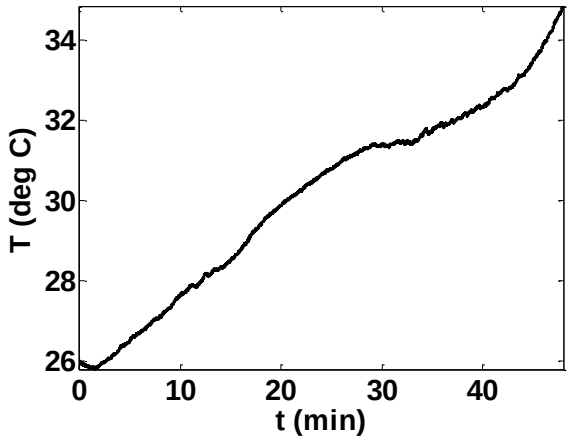

Figure 2. Temperature results for discharge current profile shown in Figure 1.

Notice the slight dip in temperature from 26°C to 25.75°C. This is not as noticeable compared to Fig. 3 in "Control Oriented Thermal Modeling of Lithium Ion Batteries," which shows a 2°C temperature dip at the beginning of the discharge. However, Figure 2 does prove the concept of an endothermic reaction causing the cell to absorb heat from the environment.

APPENDIX B.
ANSYS VALIDATION AND SIMPLIFICATION

The following appendix will document the details of multiple ANSYS simulations as well as the results and conclusions derived. The purpose of this appendix is to prove that the water temperature changes negligibly from the pipe inlet to the pipe outlet. Therefore, in "Control Oriented Thermal Modeling of Lithium Ion Batteries," we can simplify the convection model by assuming the temperature of the water is constant over the length of the pipe.

ANSYS DesignModeler was used to create a three dimensional model battery cell with aluminum plate and fluid channel. Figure 1 shows the configurations created in DesignModeler for the cell with aluminum plate to the left and fluid channel on the bottom.

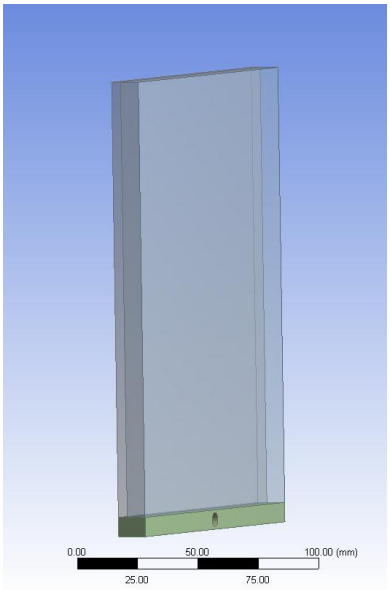

Figure 1. DesignModeler battery cell configuration with aluminum plate to the left and fluid channel on the bottom.

The geometries were imported into ANSYS CFX and the heat transfer simulation was setup. The domains were created and the material properties were assigned. The aluminum was defined as the default aluminum material provided in ANSYS CFX. The

cell material was manually created and defined as a CHT solid with a solid thermodynamic state. The cell material properties used were the following: M = 30 kg/kmol, $\rho = 3551$ kg/m^3, $c_p = 1087$ J/kgK. The cell heat source was established to be 83,333 W/m^3. This volumetric heat generation was calculated by taking a value of 0.2 W and dividing by the volume of a single node taking into account the width of the cell (i.e., the direction of heat transfer not analyzed in "Control Oriented Thermal Modeling of Lithium Ion Batteries"). Accordingly, the volumetric heat generation used in the ANSYS simulation was found using

$$\dot{Q}_v = \frac{0.2W}{0.004m \times 0.004m \times 0.15m} \tag{70}$$

The mode of heat transfer between contacting materials (i.e. between the aluminum plates and the cells) was chosen to be based on a contact thermal resistance of 1.5 x 10^{-4} W/mK. The outside surfaces are exposed to the environment at 25°C with a heat transfer coefficient of 10 W/m^{2}K. All components of the model are initialized at 25°C. The simulation is run for 3600 seconds with 10 second timesteps.

The ANSYS simulation yields the results found in Figure 2. The maximum cell temperature is 43°C and the minimum cell temperature is 32°C, yielding an 11°C temperature gradient from the top to bottom of the cell. A MATLAB simulation, similar to those described in "Control Oriented Thermal Modeling of Lithium Ion Batteries", with a constant heat generation of 0.2W and a constant fluid temperature of 25°C yielded a maximum cell temperature of 42.5°C and a minimum cell temperature of 30°C, which yields a 12.5°C cell temperature gradient.

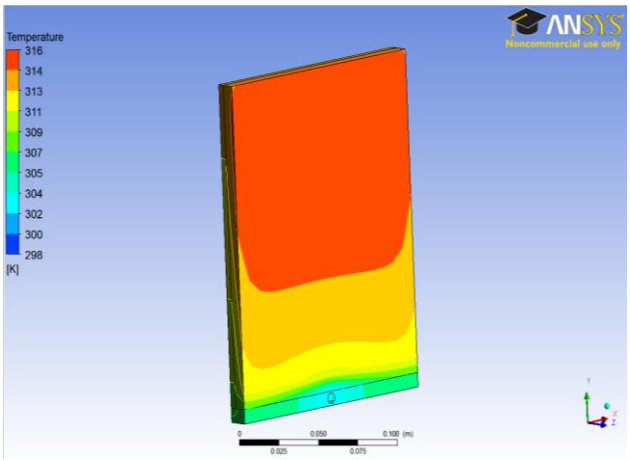

Figure 2. Single cell simulation with aluminum plates and forced convection results: maximum temperature of 43°C and cell temperature gradient of 10°C.

The results in Figure 2 yielded a change in fluid temperature from inlet to outlet of 0.2°C. A ten cell simulation with an input water temperature of 25°C was completed to determine the change in water temperature from the inlet to the outlet. The ANSYS results yielded a 1.5°C temperature gradient in the water. Therefore, the temperature of the fluid can be reasonably assumed to be a constant at 25°C.

APPENDIX C.
SYSTEM EFFICIENCY

The following appendix gives a brief insight into how the efficiency of the system used in this work is determined. The system in this work consists of a single lithium ion cell and a pump. The total power (W) of the system is

$$P_T = P_E - P_P + P_H \tag{1}$$

where P_E is electrical power generated by the cell (W), P_P is the power needed by the pump (W), and P_H is the heat generated by the cell (W). The electrical power generated by the cell is

$$P_E = V_{cell} I \tag{2}$$

where V_{cell} is the cell potential (V) and I is the current supplied to the cell (A). The cell potential was determined in the appendix of "Control Oriented Thermal Modeling of Lithium Ion Batteries" and the current supplied to the cell is 30 A. The electrical power generated over a 1C discharge can be seen in Figure 1.

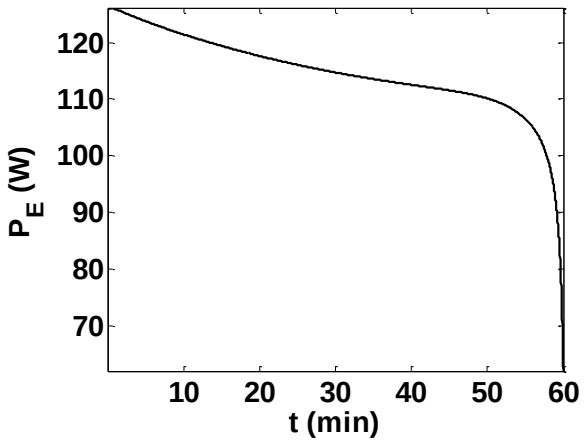

Figure 1. P_E time history for a 1C discharge rate.

The pump power (W) for this application can be determined using

$$P = \Delta p Q_f \tag{3}$$

where Δp is the pressure change (Pa) from channel inlet to outlet and Q_f is the fluid volumetric flow rate (m^3/s). The pressure change from channel inlet to outlet is [21]

$$\Delta p = fL \frac{\left(\rho \left(\frac{\dot{m}}{\rho A_{chan}} \right)^2 \right)}{2D} \tag{4}$$

where f is the friction factor, L is the channel length (m), ρ is water density (kg/m^3), $\dot{m}$ is the fluid mass flow rate (kg/s), A_{chan} is the channel area (m^2), and D is the channel diameter (m). The friction factor is [21]

$$\begin{aligned} f &= 0.316\,\mathrm{Re}_D^{-1/4} \qquad \mathrm{Re}_D \le 2\times10^4 \\ f &= 0.184\,\mathrm{Re}_D^{-1/5} \qquad \mathrm{Re}_D \ge 2\times10^4 \end{aligned} \tag{5}$$

The resulting change in pressure from channel inlet to outlet is 5.66 Pa. With a fluid volumetric flow rate of 1×10^{-5} m^3/s, the pump power is 5.66×10^{-5} W. The pump power in this application is seven orders of magnitude smaller than the electrical power generated; therefore, it is assumed that the power required by the pump is negligible. The heat generated by the cell is determined using equation (17) in "Control Oriented Thermal Modeling of Lithium Ion Batteries." The heat generated by the cell for a 1C discharge rate can be seen in Figure 2.

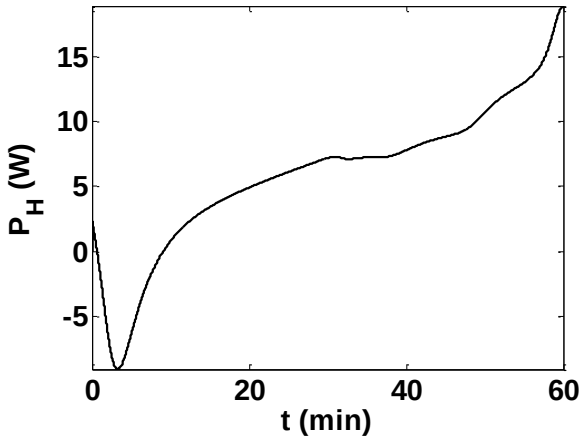

Figure 2. P_H time history for a 1C discharge rate.

The total power generated by the system is calculated from equation (1) and the results are shown in Figure 3.

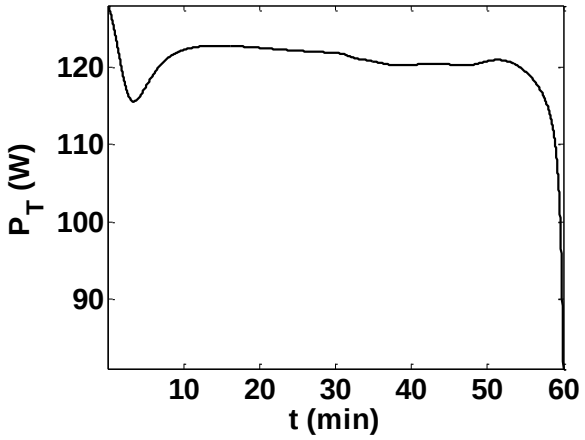

Figure 3. P_T time history for a 1C discharge rate.

The efficiency of the lithium ion cell is

$$\eta = \left(\frac{P_E}{P_T} \right) \times 100 \tag{6}$$

The cell efficiency is calculated over the 1C discharge and results can be seen in Figure 4.

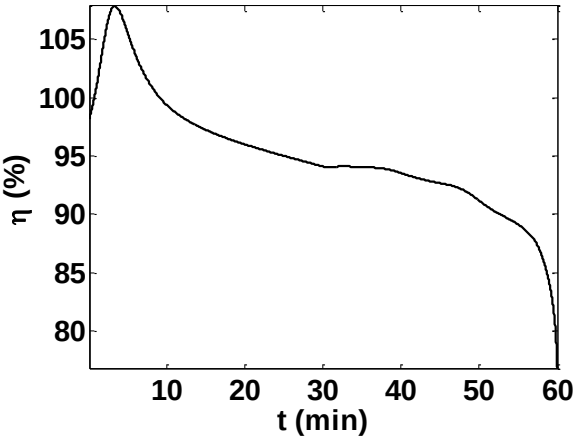

Figure 4. η time history for a 1C discharge rate.

The average cell efficiency over the discharge cycle is 95%. Notice that the cell efficiency surpasses 100% during the first ten minutes of discharge. This is due to the endothermic reaction that occurs during the first ten minutes. The endothermic reaction effects the heat generation making it negative (i.e., the cell is absorbing heat from the environment). This phenomenon can also be seen in Figure 2, where the heat generation decreases to -10W during the first ten minutes of the discharge cycle. The author suggests that this is due to the need of heat to activate the chemical reactions needed to discharge the cell.

BIBLIOGRAPHY

[1] C. Mi, B. Li, D. Buck, and N. Ota, "Advanced Electro-Thermal Modeling of Lithium-Ion Battery System for Hybrid Electric Vehicle Applications," *IEEE Vehicle Power and Propulsion Conference*, Arlington, Texas, September 9-12, 2007, pp. 107-111.

[2] X. Zhang, "Multiscale Modeling of Li-Ion Cells: Mechanics, Heat Generation, and Electrochemical Kinetics," Dissertation, The University of Michigan, Department of Mechanical Engineering, 2009.

[3] N.A. Chaturvedi, R. Klein, J. Christensen, J. Ahmed, and A. Kojic, "Algorithms for Advanced Battery-Management Systems: Modeling Estimation and Control Challenges for Lithium-Ion Batteries," *Control Systems Magazine, IEEE*, **30** (3), pp.46-68, 2010.

[4] A.A. Pesaran, "Battery Thermal Models for Hybrid Vehicle Simulations," *J. Power Sources*, **110**, pp. 377-382, 2002.

[5] R. Kizilel, R. Sabbah, J.R. Selman, and S.A. Hallaj, "An Alternative Cooling System to Enhance the Safety of Li-Ion Battery Packs," *J. Power Sources*, **194**, pp. 1105-1112, 2009.

[6] T.M. Bandhauer, S. Garimella, and T.F. Fuller, "A Critical Review of Thermal Issues in Lithium-Ion Batteries," *J. Electrochem. Soc.*, **158** (3), pp. R1-R25, 2011.

[7] P.G. Balakrishnan, R. Ramesh, and T.P. Kumar, "Safety Mechanisms in Lithium-Ion Batteries," *J. Power Sources*, **155**, pp. 401-414, 2006.

[8] V. Srinivasan and C.Y. Wang, "Analysis of Electrochemical and Thermal Behavior of Li-Ion Cells," *J. Electrochem. Soc.*, **150** (1), pp. A98-A106, 2003.

[9] W. Fang, O.J. Kwon, and C.Y. Wang, "Electrochemical-Thermal Modeling of Automotive Li-ion Batteries and Experimental Validation Using a Three-Electrode Cell," *Int. J. Energy Res.*, **34**, pp. 107-115, 2010.

[10] W.B. Gu and C.Y. Wang, "Thermal-Electrochemical Modeling of Battery Systems," *J. Electrochem. Soc.*, **147** (8), pp. 2910-2922, 2000.

[11] K.E. Thomas and J. Newman, "Thermal Modeling of Porous Insertion Electrodes," *J. Electrochem. Soc.*, **150** (2), pp. A176-A192, 2003.

[12] D. Bernardi, E. Pawlikowski, and J. Newman, "A General Energy Balance for Battery Systems," *J. Electrochem. Soc.*, **132** (1), pp. 5-12, 1985.

[13] M. Guo, G. Sikha, and R.E. White, "Single-Particle Model for a Lithium-Ion Cell: Thermal Behavior," *J. Electrochem. Soc.*, **158** (2), pp. A122-A132, 2011.

[14] M. Guo and R.E. White, "Thermal Model for Lithium Ion Battery Pack with Mixed Parallel and Series Configuration," *J. Electrochem. Soc.*, **158** (10), pp. A1166-A1176, 2011.

[15] D. Zhang, B.N. Popov, and R.E. White, "Modeling Lithium Intercalation of a Single Spinel Particle Under Potentiodynamic Control," *J. Electrochem. Soc.*, **147** (3), pp. 831-838, 2000.

[16] Y. Ma, H. Teng, and M. Thelliez, "Electro-Thermal Modeling of a Lithium-Ion Battery System," *SAE Int. J. Engines*, **3** (2), pp. 306-317, 2010.

[17] Y. Chen and J.W. Evans, "Heat Transfer Phenomena in Lithium/Polymer-Electrolyte Batteries for Electric Vehicle Application," *J. Electrochem. Soc.*, **140** (7), pp. 1833-1838, 1993.

[18] R. Bartholomaeus, C. Klaucke, and H. Wittig, "Control-Oriented Dynamic Li-Ion Battery Models for High Power Applications," *EVS24 International Battery, Hybrid and Fuel Cell Electric Vehicle Symposium*, Stravanger, Norway, May 13-16, 2009.

[19] J. Chen, S.M. Kang, J. Zou, C. Liu, and J.E. Schutt-Aine, "Reduced-Order Modeling of Weekly Nonlinear MEMS Devices With Taylor-Series Expansion and Arnoldi Approach," *J. Microelectomech. Sys.*, **13** (3), pp. 441-451, 2004.

[20] M.H. Lai, C.C. Chu, and W.S. Feng, "MIMO Interconnects Order Reductions by Using the Global Arnoldi Algorithm," *IEEE International Symposium on Circuits and Systems*, Island of Kos, Greece, May 21-24, 2006, pp. 1107-1110.

[21] F.P. Incropera, D.P. DeWitt, T.L. Bergman, and A.S. Lavine, "Introduction to Heat Transfer," John Wiley and Sons, Fifth Edition, 2007.

VITA

Derek Brown was born in St. Louis, Missouri. In May 2010, he received his B.S. in Mechanical Engineering from Saint Louis University, St. Louis, Missouri. In August 2012, he received his M.S. in Mechanical Engineering from Missouri University of Science and Technology, Rolla, Missouri.